
Article:
DerKacy, J.M., Ashall, C., Hoeflich, P. et al. (2023) JWST low-resolution MIRI spectral observations of SN 2021aefx: high-density burning in a type Ia supernova. The Astrophysical Journal Letters, 945. L2. ISSN: 2041-8205

https://doi.org/10.3847/2041-8213/acb8a8

The Astrophysical Journal Letters, 945:L2 (17pp), 2023 March 1 https://doi.org/10.3847/2041-8213/acb8a8

JWST Low-resolution MIRI Spectral Observations of SN 2021aefx: High-density Burning in a Type Ia Supernova

J. M. DerKacy[1], C. Ashall[1], P. Hoeflich[2], E. Baron[3,4], B. J. Shappee[5], D. Baade[6], J. Andrews[7], K. A. Bostroem[8,27], P. J. Brown[9], C. R. Burns[10], A. Burrow[3], A. Cikota[11], T. de Jaeger[5], A. Do[5], Y. Dong[12], I. Dominguez[13], L. Galbany[14,15], E. Y. Hsiao[2], E. Karamehmetoglu[16], K. Krisciunas[9], S. Kumar[2], J. Lu[2], T. B. Mera Evans[2], J. R. Maund[17], P. Mazzali[18,19], K. Medler[18,19], N. Morrell[20], F. Patat[6], M. M. Phillips[20], M. Shahbandeh[21], S. Stangl[3], C. P. Stevens[1], M. D. Stritzinger[16], N. B. Suntzeff[9], C. M. Telesco[22], M. A. Tucker[23,28], S. Valenti[12], L. Wang[24], Y. Yang[25,29], S. W. Jha[26], and L. A. Kwok[26]
[1] Department of Physics, Virginia Tech, Blacksburg, VA 24061, USA; jmderkacy@vt.edu
[2] Department of Physics, Florida State University, 77 Chieftan Way, Tallahassee, FL 32306, USA
[3] Homer L. Dodge Department of Physics and Astronomy, University of Oklahoma, 440 W. Brooks, Rm 100, Norman, OK 73019-2061, USA
[4] Hamburger Sternwarte, Gojenbergsweg 112, D-21029 Hamburg, Germany
[5] Institute for Astronomy, University of Hawai'i at Manoa, 2680 Woodlawn Dr., Hawai'i, HI 96822, USA
[6] European Organization for Astronomical Research in the Southern Hemisphere (ESO), Karl-Schwarzschild-Str. 2, D-85748 Garching b. München, Germany
[7] Gemini Observatory/NSF's NOIRLab, 670 North A'ohoku Place, Hilo, HI 96720-2700, USA
[8] Steward Observatory, University of Arizona, 933 North Cherry Avenue, Tucson, AZ 85721-0065, USA
[9] George P. and Cynthia Woods Mitchell Institute for Fundamental Physics and Astronomy, Texas A&M University, Department of Physics and Astronomy, College Station, TX 77843, USA
[10] Observatories of the Carnegie Institution for Science, 813 Santa Barbara Street, Pasadena, CA 91101, USA
[11] Gemini Observatory/NSF's NOIRLab, Casilla 603, La Serena, Chile
[12] Department of Physics, University of California, 1 Shields Avenue, Davis, CA 95616-5270, USA
[13] Universidad de Granada, E-18071, Granada, Spain
[14] Institute of Space Sciences (ICE, CSIC), Campus UAB, Carrer de Can Magrans, s/n, E-08193 Barcelona, Spain
[15] Institut d'Estudis Espacials de Catalunya (IEEC), E-08034 Barcelona, Spain
[16] Department of Physics and Astronomy, Aarhus University, Ny Munkegade 120, DK-8000 Aarhus C, Denmark
[17] Department of Physics and Astronomy, University of Sheffield, Hicks Building, Hounsfield Road, Sheffield, S3 7RH, UK
[18] Astrophysics Research Institute, Liverpool John Moores University, UK
[19] Max-Planck Institute for Astrophysics, Garching, Germany
[20] Las Campanas Observatory, Carnegie Observatories, Casilla 601, La Serena, Chile
[21] Space Telescope Science Institute, 3700 San Martin Drive, Baltimore, MD 21218-2410, USA
[22] Department of Astronomy, University of Florida, Gainesville, FL 32611 USA
[23] Center for Cosmology and AstroParticle Physics, The Ohio State University, 191 W. Woodruff Ave., Columbus, OH 43210, USA
[24] Department of Physics and Astronomy, Texas A&M University, College Station, TX 77843, USA
[25] Department of Astronomy, University of California, Berkeley, CA 94720-3411, USA
[26] Department of Physics and Astronomy, Rutgers, the State University of New Jersey, 136 Frelinghuysen Road, Piscataway, NJ 08854-8019, USA
Received 2023 January 9; revised 2023 February 1; accepted 2023 February 1; published 2023 February 28

Abstract

We present a JWST/MIRI low-resolution mid-infrared (MIR) spectroscopic observation of the normal Type Ia supernova (SN Ia) SN 2021aefx at +323 days past rest-frame *B*-band maximum light. The spectrum ranges from 4 to 14 μm and shows many unique qualities, including a flat-topped [Ar III] 8.991 μm profile, a strongly tilted [Co III] 11.888 μm feature, and multiple stable Ni lines. These features provide critical information about the physics of the explosion. The observations are compared to synthetic spectra from detailed non–local thermodynamic equilibrium multidimensional models. The results of the best-fitting model are used to identify the components of the spectral blends and provide a quantitative comparison to the explosion physics. Emission line profiles and the presence of electron capture elements are used to constrain the mass of the exploding white dwarf (WD) and the chemical asymmetries in the ejecta. We show that the observations of SN 2021aefx are consistent with an off-center delayed detonation explosion of a near–Chandrasekhar mass ($M_{\rm Ch}$) WD at a viewing angle of $-30°$ relative to the point of the deflagration to detonation transition. From the strengths of the stable Ni lines, we determine that there is little to no mixing in the central regions of the ejecta. Based on both the presence of stable Ni and the Ar velocity distributions, we obtain a strict lower limit of 1.2 $M_{\odot}$ for the initial WD, implying that most sub-$M_{\rm Ch}$ explosions models are not viable models for SN 2021aefx. The analysis here shows the crucial importance of MIR spectra in distinguishing between explosion scenarios for SNe Ia.

Unified Astronomy Thesaurus concepts: Supernovae (1668); Type Ia supernovae (1728); James Webb Space Telescope (2291)

[27] LSSTC Catalyst Fellow.
[28] CCAPP Fellow.
[29] Bengier–Winslow–Robertson Postdoctoral Fellow.

1. Introduction

Type Ia supernovae (SNe Ia) arise from the thermonuclear explosion of at least one carbon/oxygen (C/O) white dwarf (WD) in a binary system (Hoyle & Fowler 1960). Despite being the most precise extragalactic distance indicators in the

universe (Phillips 1993; Riess et al. 1998; Perlmutter et al. 1999; Riess et al. 2016, 2018), the exact makeups of SNe Ia progenitor systems and the mechanisms of their explosions are still unknown (see Maoz et al. 2014; Branch & Wheeler 2017; Jha et al. 2019, for recent reviews).

There are multiple progenitor scenarios that may produce SNe Ia. These include: the single-degenerate (SD) scenario, where the companion is a main-sequence star or an evolved nondegenerate companion, like a red giant or He star (Whelan & Iben 1973); the double-degenerate (DD) scenario, where the companion is also a WD (Iben & Tutukov 1984; Webbink 1984); or a triple system, where at least two of the bodies are C/O WDs (Thompson 2011; Kushnir et al. 2013). Additionally, a wide range of explosion mechanisms also exist. Multiple mechanisms originate from mergers of both stars in the progenitor system, including dynamical mergers of two WDs (Benz et al. 1990; García-Berro et al. 2017), violent mergers of two WDs (Pakmor et al. 2012, 2013), and collisions of two WDs within triple systems (Rosswog et al. 2009a; Kushnir et al. 2013). Currently, two of the leading explosion models are of SNe Ia arising from explosions of near-$M_{\rm Ch}$ mass WDs and detonations of sub-$M_{\rm Ch}$ mass WDs. In $M_{\rm Ch}$ explosions, H, He, or C material is accreted from a companion star (which can be degenerate or nondegenerate), until the central density in the primary WD is high enough to trigger a thermonuclear runaway (Iben & Tutukov 1984; Diamond et al. 2018). The flame can then propagate as a deflagration, detonation, or both, via a deflagration to detonation transition (DDT; Khokhlov 1991a; Hoeflich & Khokhlov 1996; Gamezo et al. 2003; Poludnenko et al. 2019). In contrast, a sub-$M_{\rm Ch}$ explosion is triggered when a surface He layer detonates and drives a shockwave inward, causing a secondary detonation that disrupts the whole WD (Nomoto et al. 1984; Woosley & Weaver 1994; Livne & Arnett 1995; Hoeflich & Khokhlov 1996; Shen et al. 2018). Similar to $M_{\rm Ch}$ explosions, sub-$M_{\rm Ch}$ explosions can occur in both SD and DD scenarios (Piersanti et al. 2003a, 2003b).

Due to the degenerate nature of C/O WDs, the central density (ρ_c) of the star is directly correlated with its mass (Chandrasekhar 1939). Therefore, one of the key differences between $M_{\rm Ch}$ and sub-$M_{\rm Ch}$ scenarios is the peak density of the burning. In particular, when $\rho_c > 5 \times 10^8$ g cm^{-3}, significant amounts of stable iron-group elements (IGEs), such as ^{58}Ni, are produced (Hoeflich & Khokhlov 1996). These central densities correspond to WD masses of $\gtrsim$1.2 $M_\odot$, where the thermonuclear runaway must start via compressional heating in the center of the WD (Seitenzahl & Townsley 2017).

Traditionally, there have been fewer studies of SNe Ia in the longer near-infrared (NIR) and mid-infrared (MIR) wavelengths, compared to the optical. However, recent efforts have shown that these longer wavelengths offer additional, and sometimes better, information about the physics of SN explosions (Meikle et al. 1993; Höflich et al. 2002; Marion et al. 2009; Hsiao et al. 2013; Graham et al. 2017; Diamond et al. 2018; Wilk et al. 2018; Hoeflich et al. 2021; Kumar et al. 2022; Lu et al. 2022; Hoeflich et al. 2023). This is due, in part, to the fact that the location of the photosphere is wavelength-dependent, and that different diagnostic spectral lines are revealed at longer wavelengths (Hoeflich et al. 1991; Höflich et al. 1995; Wheeler et al. 1998; Kasen 2006; Ashall et al. 2019a, 2019b).

Prior to the launch of the James Webb Space Telescope (JWST), there were only seven MIR ($\lambda > 5$ μm) spectral observations of SNe Ia across four different objects. Three spectra were obtained with the Spitzer Space Telescope: one of SN 2003hv at $\sim$+375 days (relative to the estimated explosion), one of SN 2005df at $\sim$+135 days (Gerardy et al. 2007), and one of SN 2006ce at +127 days relative to the B-band maximum light (GO-30292; PI: W. P. Meikle; Kwok et al. 2023). Four MIR spectra of SN 2014J were obtained with CanariCam on the 10.4 m Gran Telescopio Canarias, between 57 and 137 days after explosion (Telesco et al. 2015). Despite the small sample size, it is apparent that the MIR contains many diagnostics for differentiating between leading explosion scenarios. For example, nebular-phase MIR spectral observations, which probe the high-density central layers, can reveal the presence and distribution of stable Ni. These lines are direct indicators of high-density burning.

With the successful launch of JWST, high signal-to-noise ratio (S/N) MIR spectral observations during the nebular phases of SNe Ia are now possible. The first spectrum of an SN Ia obtained with JWST was that of SN 2021aefx at +255 days after maximum light (MJD = 59801.4; Kwok et al. 2023). Here, we present and analyze a spectrum of SN 2021aefx taken +323 days (MJD = 59871.6) after maximum light. In contrast to the work of Kwok et al. (2023), which focused primarily on line identifications and determinations of the observed velocities, we interpret the explosion physics of SN 2021aefx through comparisons to a self-consistent set of non–local thermodynamic equilibrium (NLTE) radiation hydrodynamic models of SNe Ia. This allows us to provide a set of line identifications that are specific to SN 2021aefx, in addition to a consistent picture of the explosion, based on our newly observed spectrum and models. In Section 2, we describe our observations, and in Section 3, we describe the details of our spectral reduction. Line identifications from the full NLTE models are performed in Section 4, while an analysis of their velocities is presented in Section 5. Section 6 discusses the details of our chosen NLTE models and presents a comparison to the observations. Alternative explosion scenarios are discussed in Section 6.4. Finally, we summarize our findings in Section 7.

2. Observations

SN 2021aefx was discovered on 2021 November 11.3 (MJD = 59529.5), by the Distance Less Than 40 Mpc Survey (Tartaglia et al. 2018), and classified as a young SN Ia (Bostroem et al. 2021; Hosseinzadeh et al. 2022). SN 2021aefx was subsequently followed by several groups, including a multiband optical and spectroscopic follow-up campaign by the Precision Observations of Infant Supernova Explosions Collaboration (POISE; Burns et al. 2021; Ashall et al. 2022).[30] POISE's detailed photometric observations revealed an early blue excess, which may be explained by a rapid change in the velocities of the spectral lines (Ashall et al. 2022). An analysis of the complete POISE data set reveals the basic light-curve properties of SN 2021aefx, including a decline rate of $\Delta m_{15}(B) = 1.01 \pm 0.06$ mag and a peak absolute magnitude of $M_B = -19.28 \pm 0.49$ mag, which places SN 2021aefx in the normal part of the luminosity–width

[30] poise.obs.carnegiescience.edu/

Table 1
JWST/MIRI Observation Details

Parameter	Value
Acquisition Image	
Filter	F1000W
Exp Time [s]	89
Readout Pattern	FASTGRPAVG8
SN 2021aefx Spectrum	
Mode	LRS
Exp Time [s]	1493
T_{obs} [MJD]	59871.6
Epoch[a] [days]	322.71
Groups per Integration	134
Integrations per Exp.	2
Exposures per Dither	1
Total Dithers	2

Note.
[a] Rest-frame days relative to *B*-band maximum of MJD = 59547.25 (C. Stevens et al. 2023, in preparation).

relation (Phillips 1993; Ashall et al. 2022; C. Stevens et al. 2023, in preparation.). SN 2021aefx is located 105″.3 south, 37″.0 west from the center of its host, NGC 1566, at a redshift of 0.005 ($\alpha = 04^h20^m00^s.42$, $\delta = -54°56'16''.10$; Allison et al. 2014). NGC 1566 is a face-on spiral galaxy with a systemic recessional velocity of 1500 km s^{-1} and a rotational velocity of 65 ± 60 km s^{-1} at the location of the SN (Elagali et al. 2019). All figures showing observed spectra of SN 2021aefx have been corrected for combined recessional and rational velocities of 1550 km s^{-1} at the location of the SN in the host. This low rotational velocity implies that any observed off-center lines (i.e., lines that are shifted relative to the line-of-sight velocity) are intrinsic to the progenitor system itself, and not attributable to a peculiar velocity within the host galaxy.

We present an MIR observation of SN 2021aefx obtained through program GO-JWST-2114 (PI: C. Ashall), from ∼4 to 14 μm. The data were obtained using JWST's Mid-Infrared Instrument (MIRI) in its Low Resolution Spectroscopy (LRS) configuration. In this mode, MIRI/LRS obtains slit spectroscopy of objects with a spectral resolving power ($R = \lambda/\Delta\lambda$) of $R \sim 100$ at 7.5 μm, varying from $R \sim 40$ at 5 μm to $R \sim 160$ at 10 μm (Kendrew et al. 2015; MacEwen et al. 2016; Rigby et al. 2022). The instrumental configuration is identical to that of Kwok et al. (2023). The spectral observations were performed with a two-point dither strategy. For each grating setting, there were 134 groups per integration, two integrations per exposure, and one exposure per dither. This results in an exposure of 734.5 s at each dither position, and these are combined for a total exposure time of 1493 s. Full details of our observational setup are found in Table 1.

3. Data Reduction

The data were obtained on 2022 October 19.6 (MJD = 59871.6) and reduced with the JWST calibration pipeline,[31] version 1.8.1 (Bushouse et al. 2022). Both the raw (Stage 1 calibrated) and fully reduced data were retrieved from the Mikulski Archive for Space Telescopes (MAST).[32] These data can be accessed via DOI 10.17909/6fjc-sx91. The raw data were processed with a local installation of version 1.8.1 of the pipeline, for comparison to the fully reduced data from MAST, using the `spec_mode_stage_2` and `spec_mode_stage_3` Jupyter notebooks as templates for the reduction. Both reductions used the most up-to-date wavelength (jwst_miri_specwcs_0005.fits) and flux calibration (jwst_miri_photom_0085.fits) files. These calibration files produce a wavelength solution that is accurate to ∼0.05–0.02 μm, varying from short to long wavelengths, and a flux calibration that is accurate to a ∼2%–5% global offset between 5 and 12 μm (Gordon et al. 2022; S. Kendrew, private communication). Furthermore, Kwok et al. (2023) found that the flux calibration of their MIRI spectrum was accurate to 2%.

Using the LRS Optimal Spectral Extraction notebook,[33] the spectra were re-extracted using multiple techniques. This re-extraction was necessary to properly center the positions of the spectra in the science aperture, as the pipeline-derived aperture produced poor extraction at long wavelengths. After the proper re-extraction with the Optimal Extraction notebook, no significant differences were found between the locally reduced data and the fully calibrated (but unextracted) data available from MAST. Future updates to the JWST calibration files are expected to further improve the accuracy of the automated extractions (S. Kendrew, private communication).

4. Data Comparison and Line Identifications

Figure 1 presents the spectrum of SN 2021aefx acquired on 2022 October 19.6 (corresponding to +323 days after the *B*-band maximum light), from 4 to 14 μm. At these phases, the ejecta are optically thin and dominated by emission lines. The strongest of these lines are labeled in Figure 1. Figure 2 shows our spectrum of SN 2021aefx compared to the MIR spectra of SNe 2005df (Gerardy et al. 2007), 2006ce (Kwok et al. 2023), and 2014J (Telesco et al. 2015), as well as the earlier spectrum of SN 2021aefx at +255 days (Kwok et al. 2023). From Figure 2, it is clear that SN 2021aefx is similar to other previously observed SNe Ia, but the size and sensitivity of JWST produces a high-S/N spectrum with a quality that was previously impossible to obtain. Comparing the two JWST spectra of SN 2021aefx, the most noticeable difference is the decrease in the relative strength of the ∼11.9 μm profile compared to the other features, caused by the radioactive decay of ^{56}Co.

To assist in the line identifications, we use a suite of full NLTE radiation transport models. These models reproduce both the early- and late-time properties of SN 2021aefx, and an in-depth discussion of the models with respect to the MIR observables can be found in Section 6.

A detailed examination of the SN 2021aefx MIR spectrum reveals four prominent wavelength regions of line formation, which are described individually in the following subsections. Detailed line identifications in each of these regions are plotted in Figure 3, while Table 2 lists the lines that contribute significantly to the spectrum.

4.1. The 6.0–8.0 μm Region

The 6.0–8.0 μm region is dominated by emission lines of stable Ni, the most prominent of which is a blend of

[31] https://jwst-pipeline.readthedocs.io/en/stable/jwst/introduction.html
[32] https://mast.stsci.edu/portal/Mashup/Clients/Mast/Portal.html
[33] https://spacetelescope.github.io/jdat_notebooks/notebooks/MIRI_LRS_spectral_extraction/miri_lrs_spectral_extraction.html

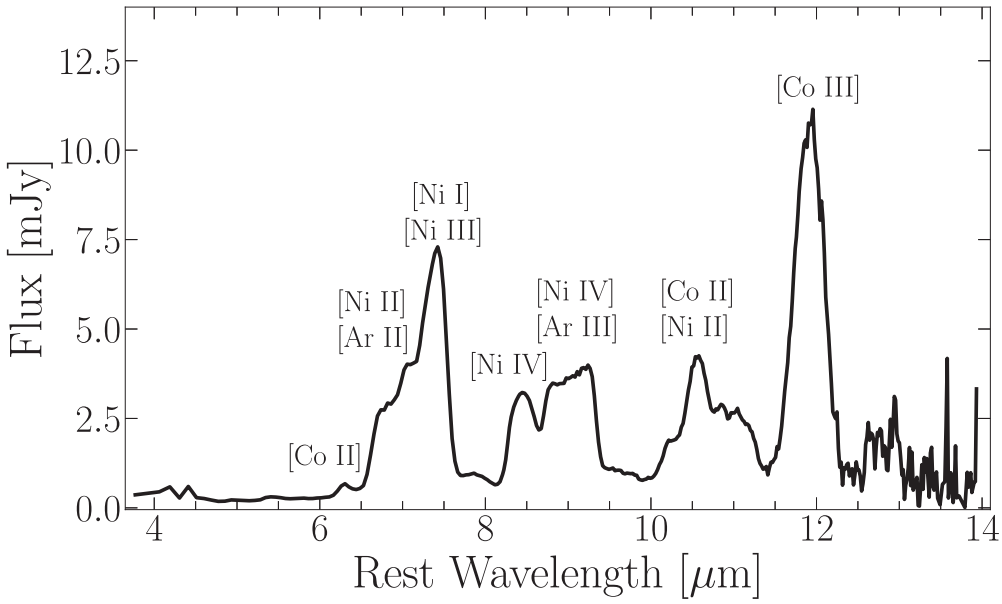

Figure 1. JWST/MIRI LRS spectrum of SN 2021aefx at +323 days relative to the *B*-band maximum. The ions responsible for the most prominent features in the spectrum are labeled. A full set of line identifications is plotted in Figure 3 and shown in Table 2.

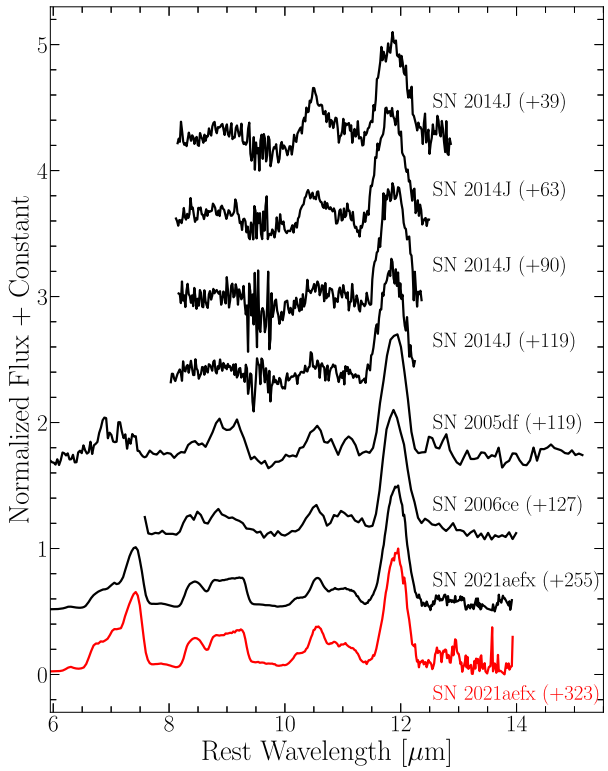

Figure 2. Comparison of the +323 day spectrum of SN 2021aefx to other MIR spectral observations of SNe Ia, including SNe 2005df (Gerardy et al. 2007), 2006ce (Kwok et al. 2023), and 2014J (Telesco et al. 2015), as well as the +255 day spectrum of 2021aefx (Kwok et al. 2023). The epoch relative to the *B*-band maximum light for each spectrum is shown. The primary difference between the +255 and +323 day spectra of SN 2021aefx is the increased strength of the other features relative to the peak at ∼11.9 μm.

[Ni III] 7.349 μm and [Ni I] 7.507 μm that defines the red edge of the feature. The blue edge of this peak is blended with several other weaker lines, creating a series of shoulders, extending from ∼6.5 to ∼7.2 μm. Moving from red to blue, these shoulders are comprised of [Ar II] 6.985 μm, [Ni II] 6.920 μm, and [Ni II] 6.636 μm. Finally, there is a small bump that is associated with a combination of [Co II] 6.214 μm, [Co I] 6.273 μm, and [Co II] 6.274 μm.

4.2. The 8.0–9.5 μm Region

The 8.0–9.5 μm region is dominated by two features whose edges are blended with other weaker lines at ∼8.7 μm. The bluer of the two is due to the emission of [Ni IV] 8.405 μm, while the redder feature is dominated by the [Ar III] 8.991 μm line. The [Ar III] line shows a distinct flat-topped profile, which increases in flux from blue to red. Tilted flat-topped profiles are connected to both an ion's velocity distribution in the ejecta and the viewing angle of the explosion (see Sections 5.1 and 6.3.1, as well as Hoeflich et al. 2021). Small contributions from the weak [Fe II] 8.733 μm and [Ni IV] 8.945 μm lines may also add to the observed flux at the 10% level.

4.3. The 9.5–11.5 μm Region

The 9.5–11.5 μm region shows a structure reminiscent of the 6.0–8.0 μm region, with one dominant blended feature and a series of smaller bumps and shoulders blended into the wings. The strongest peak arises from a blend of [Co II] 10.523 μm and [Ni II] 10.682 μm. A blend of [Fe II] 10.189 μm and [Fe III] 10.203 μm forms a shoulder that is partially blended into the blue wing of the [Co II]+[Ni II] blend. Blended into the red wing is a series of three other weaker features. The first feature, centered near ∼10.85 μm, is not associated with any strong lines in our model. The next feature in the series arises from the comparatively weak [Ni III] 11.002 μm line, while a blend of [Ni IV] 11.130 μm and [Co II] 11.167 μm forms a shoulder on the red wing of the [Ni III] line. Finally, there may be a small contribution to the red wing of the [Ni IV]+[Co II] shoulder from [Ni I] 11.307 μm.

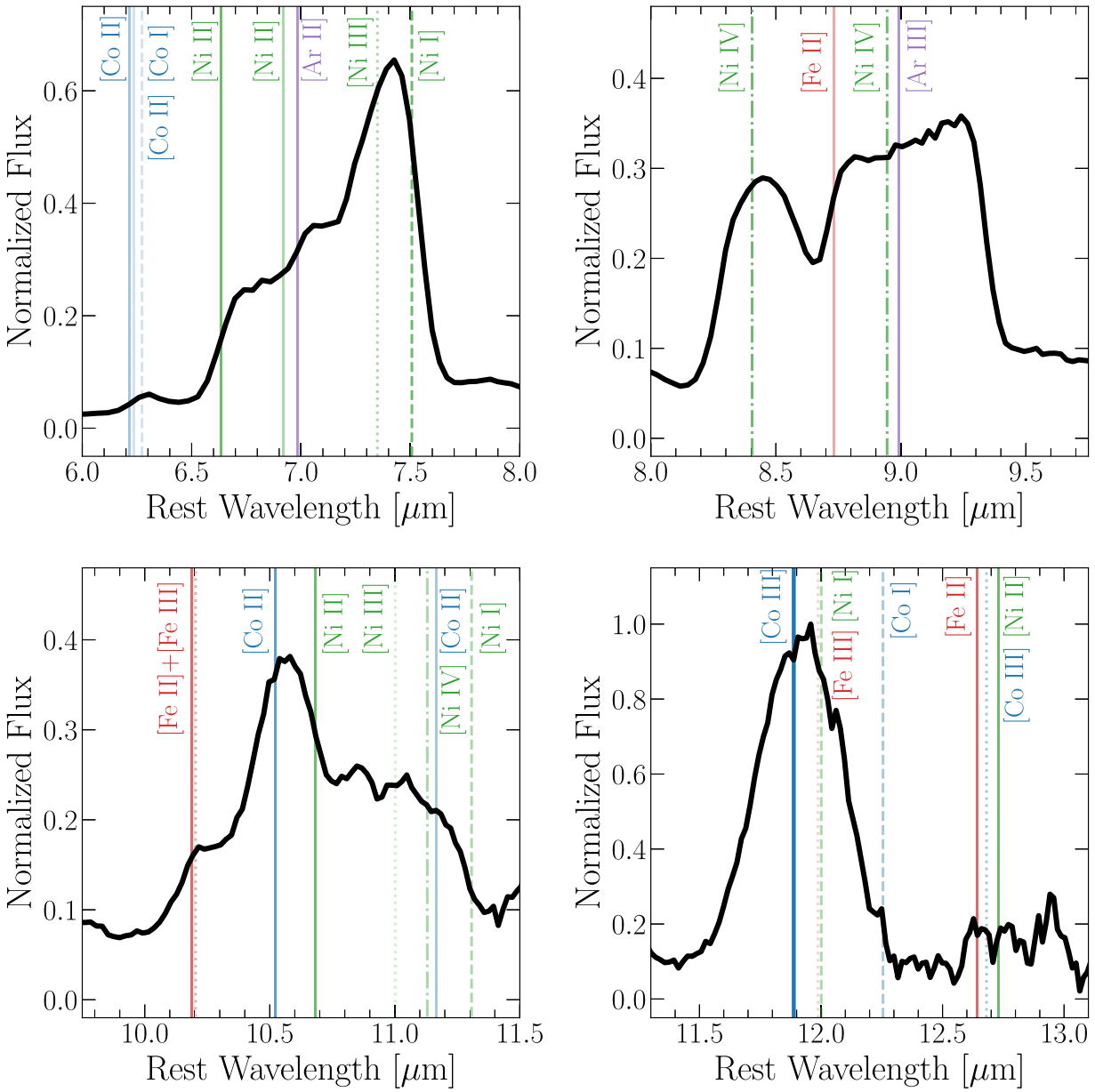

Figure 3. Detailed line identifications in the four prominent feature regions, based on the lines from Model 25 (Hoeflich 2017) that are included in Table 2. The color intensities of the vertical lines correspond to the strengths of the spectral lines, with four-star lines being the most intense and one-star lines being the faintest. The dashed lines correspond to ground-state ions, the solid lines to singly ionized species, the dotted lines to doubly ionized species, and the dashed–dotted lines to triply ionized species.

4.4. The 11.5–13.0 μm Region

The 11.5–13.0 μm region contains the only relatively isolated unblended feature in the MIR spectrum, the [Co III] 11.888 μm resonance line, which produces the strongest line in the entire MIR spectrum. Our model shows weak contributions from [Fe III] 11.978 μm and [Ni I] 12.001 μm, but they only produce $\sim$1% of the flux and do not alter the line profile in a significant manner (again, see Table 2). A small shoulder at the edge of the red wing of the [Co III] line is attributable to [Co I] 12.255 μm. A series of peaks between 12.5 and 13.0 μm suggests the presence of multiple weak lines, but the low S/N in this region prevents us from unambiguously identifying any lines. We tentatively identify the first peak with [Fe II] 12.642 μm and [Co III] 12.681 μm, and the second peak with [Ni II] 12.729 μm. Our model shows no strong lines in the vicinity of the third and final peak in the series.

5. Velocity Distributions and Line Profiles

In this section, we discuss the velocity distributions and line profiles of three important species in the ejecta: Ar, Co, and Ni. In discussing these velocities and profiles, we reiterate that the current wavelength calibration of the MIRI/LRS observations is accurate to 0.05–0.02 μm, with lower errors at longer wavelengths. This corresponds to errors on the order of $\sim$500 km s^{-1} in the [Co III] 11.888 μm line and $\sim$1400 km s^{-1} in the [Ni III] 7.349 μm line. Future updates to the JWST pipeline calibration files may increase the precision of these results.

5.1. [Ar III] 8.991 μm

Ar traces the transition region between incomplete oxygen burning and nuclear statistical equilibrium (NSE) in the ejecta,

Table 2
MIR Line Identifications from Model 25

S	λ (μm)	Ion	S	λ (μm)	Ion
**	6.214	[Co II]		8.555	[Fe III]
*	6.273	[Co I]	**	8.611	[Fe III]
*	6.274	[Co II]	*	8.644	[Co II]
**	6.383	[Ar III]	**	8.733	[Fe II]
***	6.636	[Ni II]	**	8.945	[Ni IV]
	6.636	[Ni II]	***	8.991	[Ar III]
**	6.920	[Ni II]	*	9.618	[Ni II]
***	6.985	[Ar II]	*	10.080	[Ni II]
	6.985	[Ar II]	***	10.189	[Fe II]
	6.985	[Ar II]	**	10.203	[Fe III]
	7.045	[Co I]	***	10.523	[Co II]
	7.103	[Co III]	***	10.682	[Ni II]
	7.147	[Fe III]	*	11.002	[Ni III]
	7.272	[Fe III]	**	11.130	[Ni IV]
**	7.349	[Ni III]	**	11.167	[Co II]
***	7.507	[Ni I]	**	11.307	[Ni I]
	7.773	[Co I]	****	11.888	[Co III]
***	7.791	[Fe III]	*	11.978	[Fe III]
*	8.044	[Co II]	**	12.001	[Ni I]
*	8.063	[Ni II]	**	12.255	[Co I]
	8.114	[Co I]	*	12.261	[Mn II]
**	8.211	[Fe III]	***	12.642	[Fe II]
	8.282	[Ni I]	**	12.681	[Co III]
***	8.405	[Ni IV]	***	12.729	[Ni II]
**	8.489	[Co III]		13.058	[Co I]

Note. For each transition, the markers correspond to dominant (****), strong (***), moderate (**), weak (*), and scarcely detectable ( ), on top of the quasi-continuum formed by a large number of lines. The relative strength S is estimated by the integral over the envelope, $\int A_{ij} n_j \, dV$, where n_j is the particle density of the upper level. The list is based on the simulations described in Section 6.

thereby providing details about the chemical distribution between the ^{56}Ni and Si-group layers. The [Ar III] 8.991 μm line profile is plotted in Figure 4 in velocity space. The profile is flat-topped, with an increasing tilt from blue to red wavelengths, which we hereafter refer to as a "flat-tilted" profile. Flat-topped profiles are indicative of a central hole or void in the emitting material—that is, a shell of line-emitting material (Beals 1929; Menzel 1929; Struve 1931). For [Ar III], the flat-top component of the feature starts at ~ -7000 km s^{-1} and extends to $\sim$8000 km s^{-1}. The feature increases in flux by 10% across the profile, from the blue to the red side, and the flat-topped component of the profile indicates that there is a central hole in the ejecta of $\sim \pm 8000$ km s^{-1} that does not contain Ar. This is because Ar is destroyed in high-temperature regimes of the NSE, where $T \geqslant 6 \times 10^9$ K, and there is a lack of strong mixing during the explosion, consistent with explosion models of near-$M_{\rm Ch}$ WDs (see Section 6 for details).

5.2. [Co III] 11.888 μm

SNe Ia are powered by a nuclear decay chain of ^{56}Ni to ^{56}Co to ^{56}Fe. Since the [Co III] 11.888 μm feature is a resonance line, most of the de-excitation and recombination of Co passes through this transition, making it a direct tracer of the distribution and amount of ^{56}Ni in the ejecta. This feature covers a width of $\sim \pm$10,000 km s^{-1}. If the shape of the line is assumed to be symmetric, and thus well described by a Gaussian profile, it peaks at 740 ± 200 km s^{-1}, with an FWHM

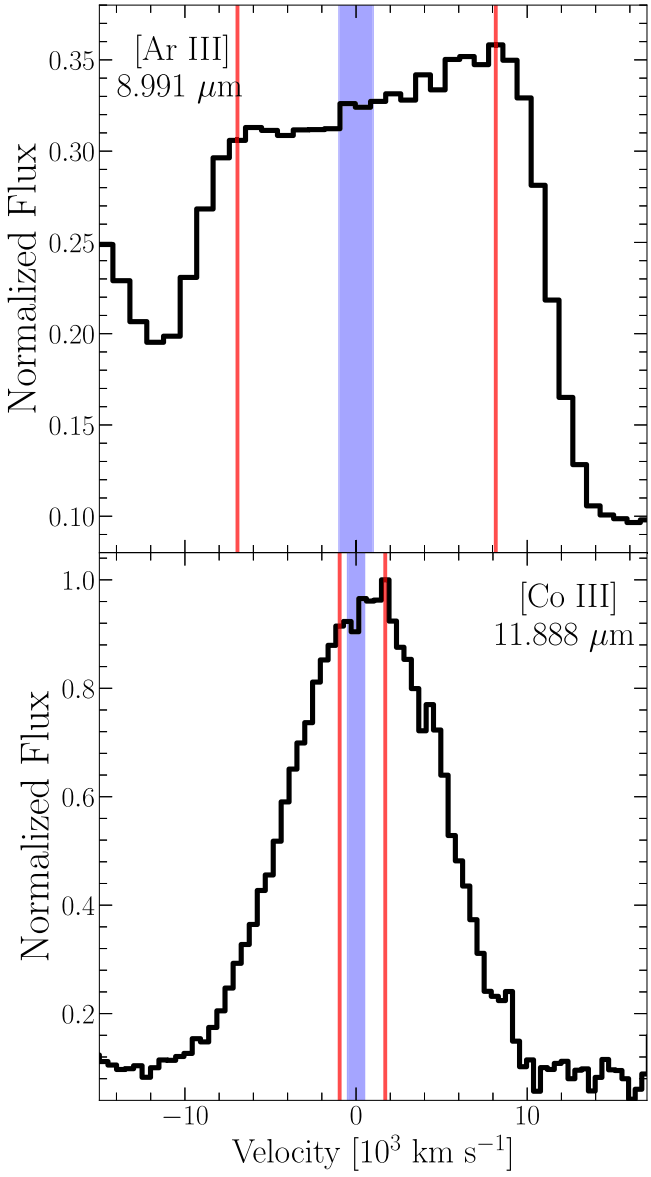

Figure 4. Line profiles of the [Ar III] (top) and [Co III] lines (bottom) in velocity space. The blue boxed region around $v = 0$ km s^{-1} in the rest frame denotes the 1σ error in the rest wavelength for the given line. The red vertical lines mark the left and right edges of the flat-tilted profiles in both panels.

of 4840 ± 170 km s^{-1} (see Figure 5). Combining the error in the line-of-sight velocity (recessional plus rotational; $\sim$60 km s^{-1}) and the estimated error in the wavelength calibration of $\sim$500 km s^{-1} with that of the fit error yields a total estimated error of 544 km s^{-1}. The fact that this resonance line is not located at the kinematic center of the explosion indicates that the bulk of the ^{56}Ni is off-center, at the 1.4σ level. The [Co III] 11.888 μm profile also shows hints of a flat-tilted profile, peaking to the red at $\sim$2000 km s^{-1} (see Figure 4), although the low resolution prevents a definitive identification of this profile. Similarly, hints of this flat-tilted peak are also seen in the spectrum at an earlier epoch of SN 2021aefx (see Kwok et al. 2023). If real, this flat-tilted profile may extend from ~ -1000 to $\sim$2000 km s^{-1}. Similar to the [Ar III] 8.991 μm line, the flat-tilted profile of the [Co III] feature may imply a central hole of ^{56}Ni in the ejecta. This hole would be smaller than that of Ar, and would only be a few thousand kilometers per second across

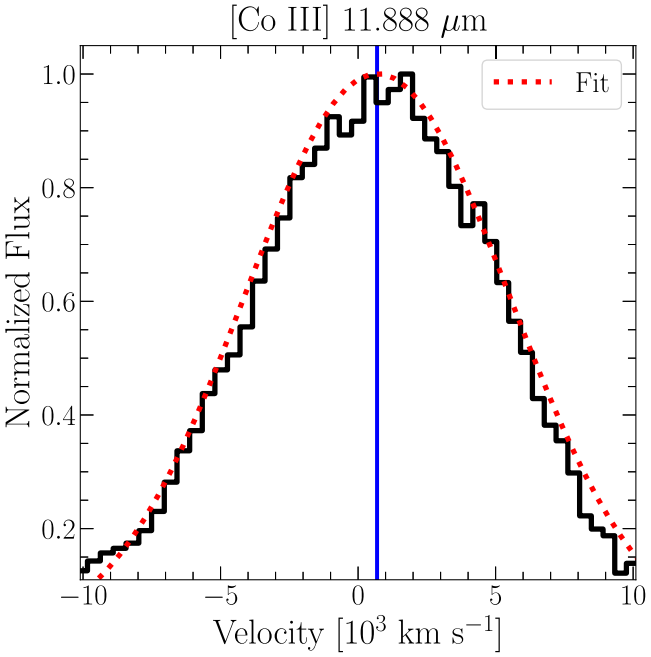

Figure 5. The [Co III] 11.866 μm line compared to a Gaussian fit. The Gaussian peaks at 11.91 ± 0.01 μm, $\sigma = 0.19 \pm 0.04$ μm, which in velocity space corresponds to a peak at 740 ± 200 km s^{-1} and $\sigma = 4840 \pm 170$ km s^{-1}.

(Diamond et al. 2015; Telesco et al. 2015). Note that unlike Ar, which is produced by nuclear burning and has a steep temperature dependence, leading to a sharp cutoff in velocity extent and thus flat line profiles, electron capture (EC) is nearly temperature-independent, so its effects follow the density profile, leading to somewhat rounder line profiles. The increase in flux across the [Co III] 11.888 μm profile is 10%, the same as that in the [Ar III] 8.991 μm feature, implying that the distributions of the two elements are linked. Since Ar is produced at the edge of the ^{56}Ni region (see Section 6), it is reasonable that Ar and Co have similar changes in flux across their profiles. In Section 6, we discuss the [Co III] 11.888 μm line profile in the context of off-center ^{56}Ni distributions in the explosion. However, in order to confirm that the [Co III] 11.888 μm feature is truly asymmetrical and off-center higher-resolution spectra will be required—such as those obtainable by the Medium Resolution Spectrograph (MRS) of JWST/MIRI—and improved wavelength calibrations will also be needed.

5.3. Stable Ni

Multiple ionization states of Ni have forbidden emission lines that occur in the MIR, making nebular-phase MIR spectra an invaluable resource for probing the explosion physics and corresponding nucleosynthesis of SNe Ia. Since the ^{56}Ni that powers the early light curves of SNe Ia has a half-life of 6.1 days, any emission from Ni at these late phases comes from isotopes of stable Ni (e.g., ^{58}Ni), and not from radioactive isotopes like ^{56}Ni. Figure 6 presents three of these regions in velocity space. The left panel shows the [Ni III] 7.349 μm line, which appears to be redshifted in velocity space, with an apparent maximum around 3000 km s^{-1}. However, this feature is blended with [Ni I] 7.506 μm, such that the velocity extent of [Ni III] 7.349 μm appears to be larger than its true distribution. The middle panel shows the [Ni III] 8.405 μm line profile in velocity space, while the right panel depicts the [Ni III] 11.002 μm feature within a much larger series of blended lines. At higher resolution, these blends, including the 11.002 μm line, are likely to be resolved.

6. Numerical Modeling and Implications for Explosion Scenarios

To explore the explosion physics of SN 2021aefx, we turn to detailed comparisons with NLTE radiation hydrodynamical models. The goals of these comparisons are: (1) to demonstrate that MIR spectral features and line profiles can be used as critical tools for determining the explosion physics and progenitor scenario of SNe Ia; and (2) to show that JWST has opened up a new frontier in MIR SN science and demonstrate that there is a need to test and calculate atomic models and processes, including cross sections, to improve future models. Specifically, we address how the data allow us to measure the mass of the exploding WD, the chemical asymmetries in the initiation of the explosion, and small-scale mixing processes in the ejecta. When taken in total, these measurements allow us to determine the most likely explosion scenario of SN 2021aefx.

As discussed in Section 5.3 and shown by Kwok et al. (2023), SN 2021aefx presents many spectral lines of stable Ni (Figure 3). This Ni requires high-density burning in the ejecta, above 5×10^8 g cm^{-3}, which must originate from a massive WD, making the explosion either a near-$M_{\rm Ch}$ WD, where the explosion is triggered by compressional heating in the center of the explosion, or the detonation of a high-mass, sub-$M_{\rm Ch}$ WD, larger than 1.15–1.2 $M_\odot$ (Hoeflich & Khokhlov 1996; Höflich et al. 1998; Seitenzahl & Townsley 2017; but see also Blondin et al. 2022). Such massive WDs can only be produced via accretion (Kippenhahn et al. 2013). Therefore, we limit our comparisons to models within this region of parameter space.

6.1. Numerics

The simulations employ modules of the HYDrodynamical RAdiation (HYDRA) code. HYDRA solves the time-dependent radiation transport equation and positron transport (Penney & Hoeflich 2014), including the rate equations that calculate the nuclear reactions, based on a network with 211 isotopes and statistical equations for the atomic-level populations, the equation of state, the matter opacities, and the hydrodynamic evolution, as applied to SN 2020qxp (Hristov et al. 2021; Hoeflich et al. 2021, and references therein). The detailed atomic models and line lists are based on the database for bound–bound transitions of Van Hoof (2018),[34] supplemented by additional forbidden lines from Diamond et al. (2015) and Telesco et al. (2015). For details on the modeling of nebular-phase spectra with HYDRA, see Hoeflich et al. (2021), and for more general discussions on modeling the nebular phase and downward cascading of high-energy particles and photons using Monte Carlo, see also Spencer & Fano (1954), Axelrod (1980), Kozma & Fransson (1992), Fransson (1994), Mazzali et al. (2007), Fransson & Jerkstrand (2015), Mazzali et al. (2015), Botyánszki & Kasen (2017), Wilk et al. (2018), Shingles et al. (2020), and Wilk et al. (2020). The models include transitions for ionization stages I–IV of C, O, Ne, Mg, Si, S, Cl, Ar, Ca, Sc, Ti, V, Cr, Mn, Fe, Co, and Ni. Though most of the prominent features in the MIR are caused by forbidden lines, the underlying quasi-continuum is formed by

[34] Version v3.00b3: https://www.pa.uky.edu/~peter/newpage/.

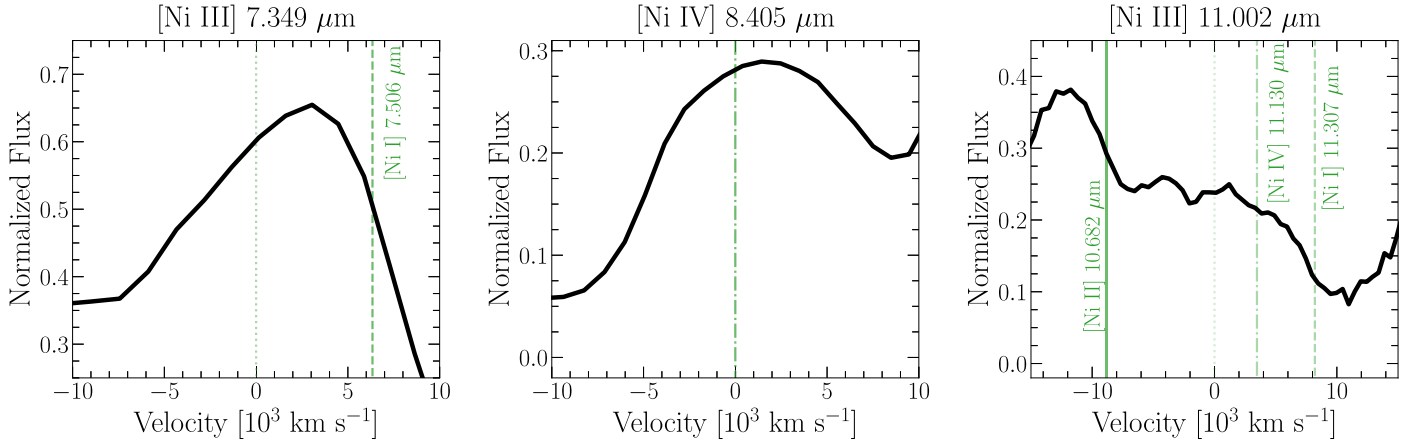

Figure 6. Velocity space profiles of the three spectral regions with prominent Ni lines. The vertical lines indicate the ionization and line strength, as in Figure 3. The left panel shows that the [Ni III] 7.349 μm region is contaminated by the [Ni I] 7.506 μm feature. The right panel, centered on the [Ni III] 11.002 μm line, shows evidence for multiple stable Ni lines contributing to the series of weak features and shoulders.

allowed lines in the inner layers well above the critical density. At these phases, the iron-rich layers are still partially optically thick at UV wavelengths, meaning the inclusion of permitted lines is important for fully characterizing the ionization balance via Rosseland cycles (Mihalas 1978).

6.2. A Delayed Detonation Model for SN 2021aefx

We compare SN 2021aefx to new simulations of off-center $M_{\rm Ch}$ mass explosion models, based upon the spherical model of the Model 25 series from Hoeflich (2017), as it produces early light-curve properties and a maximum light luminosity very similar to those of SN 2021aefx. These new simulations are parameterized explosion models, using a spherical delayed detonation to constrain the global parameters of the explosion. Fine-tuning these models is not necessary to achieve the goals of this study, as we focus on spectra, rather than high-precision photometry. The model produces $\Delta m_{15}(V) = 0.68$ mag (for reference, $\Delta m_{15}(V) = 0.64 \pm 0.01$ mag for SN 2021aefx, which is within the error of the model) and $\sim 0.6\,M_{\odot}$ of ^{56}Ni.

The model originates from a C/O WD with a main-sequence progenitor mass of 5 $M_{\odot}$, solar metallicity, and a central density $\rho_c = 1.1 \times 10^9$ g cm^{-3}. We adopt this ρ_c due to the line width and shape of the [Co III] 11.888 μm line and due to the strength of the stable Ni lines in the MIR spectrum (see Section 5.3). In this model, burning starts as a deflagration front near the center and transitions to a detonation (Khokhlov 1991b). The DDT is triggered when the density at the burning front drops below 2.5×10^7 g cm^{-3}, when $\sim 0.24\,M_{\odot}$ of the material has been burned by the deflagration front, and is induced by the mixing of unburned fuel and hot ashes (Khokhlov 1991b). The model has a magnetic field of B(WD) = 10^6 G, which has been found in magnetohydrodynamical simulations, suggesting that turbulent magnetic fields are produced during the deflagration phase (Diamond et al. 2018; Hristov et al. 2021). The basic model parameters are given in Table 3.

6.2.1. Off-center ^{56}Ni and Abundance Distributions

To investigate the line profiles and asymmetries, we consider the Model 25 series that includes off-center DDTs. For the construction of the off-center DDT, we follow the description of Livne (1999) that has also been employed by Höflich et al. (2006), Fesen et al. (2015), Hoeflich et al. (2021), and Hoeflich et al. (2023). The DDT is triggered at $M_{\rm DDT} = 0.5$ $M_{\odot}$. Note that due to the buoyancy of the flame fronts in the explosion, the DDT can be triggered at a different mass coordinate relative to the total integrated mass of the deflagration burning. This leads to asymmetric abundance distributions of all the elements produced during the detonation phase (see Figure 2 in Hoeflich et al. 2021).

In principle, the use of multiple resolved line profiles allows us to determine the value of $M_{\rm DDT}$, as well as the viewing angle. In the case of SN 2021aefx, we use the two strongest features: [Co III] 11.888 μm and [Ar III] 8.991 μm. As shown in Figure 4, we see a consistent tilt in the [Ar III] and [Co III] lines. We can determine the viewing angle from the tilt of these features. The value of $M_{\rm DDT}$ determined here is also consistent with the spectrophotometric observations of the normal SN Ia 2019np (Hoeflich et al. 2023). Most normal SNe Ia have very similar polarization properties (Cikota et al. 2019).

6.2.2. Overall Abundance Distribution

The angle-averaged abundance structure and the ^{56}Ni distribution of Model 25 are shown in Figure 7. In the model, the region of high EC is spherical, because we assume central ignition, no fragmentation during the ^{56}Ni decay in the first week after the explosion (e.g., Fesen et al. 2015), and that Rayleigh–Taylor instabilities are largely suppressed by high magnetic fields (Hristov et al. 2018). The most notable results in the abundance distribution are: (1) $\sim 6 \times 10^{-2} M_{\odot}$ of ^{58}Ni is produced in the center of the ejecta; (2) the velocity extent of the central hole in ^{56}Ni is $\sim$3200 km s^{-1}; (3) the velocity extent of the ^{56}Ni region produced in NSE ranges from $\sim$3200 to 10,000 km s^{-1}; and (4) the size of the shell of the Ar region covers a range of $\sim$8000–15,000 km s^{-1}. We note that simulating the point of the DDT in multiple dimensions does not lead to a strong rarefaction wave (Gamezo et al. 2005; Fesen et al. 2015), as seen in all spherical delayed detonation models (Khokhlov 1991b; Höflich et al. 2002; Hoeflich et al. 2021).

The off-center DDT at a point in an already expanding medium results in a run time effect that yields an asymmetric distribution of burning products. The material closer to the DDT burns under higher density than the opposite side, because the front reaches the corresponding layer 0.5–1 s later. The result is a bulge of all elements that undergo only Si and O

Table 3
Model 25 Parameters

Parameter	Value
M_{ej}	$\sim 1.38\ M_{\odot}$
ρ_c	1.1×10^9 g cm^{-3}
M_{tr}	$0.24\ M_{\odot}$
M_{DDT}	$0.5\ M_{\odot}$
B(WD)	10^6 G

burning, including Ca, Ar, and ^{56}Ni (see Figure 7). For a more complete depiction of this, see Figure 7 of Fesen et al. (2007). These asymmetries are aligned along the axis defined by the center and the DDT ignition point.

6.3. Spectral Modeling

6.3.1. Determining the Inclination Angle

We begin our discussion of Model 25's fit to the observations by illustrating its ability to determine the inclination angle of the explosion relative to our line of sight. Remember that to first order, the [Co III] profile can be fit with a Gaussian of half-width $\approx$4800 km s^{-1}, emission wings ranging from $-$10,000 to +10,000 km s^{-1}, and an offset from the rest wavelength of +740 km s^{-1} (see Section 5 and Figure 5). This is consistent with the overall ^{56}Ni distribution seen in the model (see Figure 7), but we note that by assuming an emission feature is a Gaussian we are making an implicit assumption about the underlying chemical distribution of an element within the ejecta, so caution should be exercised. As previously discussed, the host galaxy is seen face on and it has a very small projected rotation (65 ± 60 km s^{-1}), implying that host rotation plays a minor role in this offset. This leaves the peculiar motion of the progenitor system and the orbital velocity of the progenitor as the remaining potential sources of this offset. However, if these were the dominant factors, one would expect a consistent velocity offset in all the spectral lines, contrary to the observations.

On the other hand, the observed flux in the [Co III] 11.888 μm line center changes by $\sim$10% across the peak of the feature (see Section 5), consistent with expectations for the flux arising from the asymmetric ejecta of an off-center DDT model, when viewed from a specific angle (Hoeflich et al. 2021). As previously shown in Section 5, the [Co III] 11.888 μm feature appears to show a flat-tilted profile, where the velocity extent of the central tilted region corresponds to the region in velocity space of partial burning in quasi-statistical equilibrium (QSE; $\approx$1800 km s^{-1} across in the angle-averaged spectrum). This flat-tilted profile is seen in both the +255 and +323 day JWST spectra. In Model 25, the inner size of the EC region and the distribution of the ^{56}Ni produce different line profiles, when viewed at different angles. Three specific viewing angles ($-90°$, $-30°$, and $+30°$) are shown in Figure 8. From the bottom left panel, we see that the observations are well matched by a viewing angle of $\approx -30°$, including the replication of the $\sim$10% change in flux across the peak seen in the observations. While the high S/Ns ($\approx$ 100) of both JWST spectra of SN 2021aefx suggest that the flat-tilted profile is real and significant, future planned observations with JWST/MIRI MRS (JWST-GO-2114; PI: C. Ashall) will better resolve the line profiles.

6.3.2. Overall MIR Spectra

Having determined the inclination angle, we now compare our full model spectrum to our observations, as seen in Figure 9. The model spectra are shown with and without the mixing of EC elements on the scale of the pressure scale height of the WD (Höflich & Stein 2002). We examine microscopic mixing (i.e., smaller than the mean free path of the positrons) in the center of the explosion, to constrain the position (e.g., central, off-center, or multispot) of the thermonuclear runaway ignition (Nienmeyer et al. 1996; Höflich & Stein 2002; Calder et al. 2004; Livne et al. 2005; Röpke et al. 2007; Ma et al. 2013).

The most dominant lines produced by the models are shown in Table 2, and they have been successfully identified in Figure 3. For NIR lines outside the observed range, see the Appendix. Identifications of weaker lines within the spectrum will be possible after the acquisition of MIRI/MRS data.

The model reproduces the observations overall, including all four regions of prominent spectral lines, and it does especially well in reproducing the blends of the 6.0–8.0 μm and 8.0–9.5 μm regions in addition to the [Co III] 11.888 μm line. While the exact contributions of each ion may vary with the underlying explosion model, the synthetic spectra have been obtained without further tuning, and in general they are in good agreement with the observations. The similarities between the mixed and unmixed models show the stability of the synthetic spectral features.

Most of the Ni features are in blends with other IGEs of similar strengths. In light of the uncertainties in the atomic models and cross sections, the photons at a given wavelength may couple to elements other than Ni (through fluorescence; Morrison & Sartori 1966). Thus, many of the line IDs of the weaker features in low-resolution spectra are model-dependent. The easiest way to separate the elements is by comparing the mixed and unmixed models. In the unmixed models, the EC elements are effectively shielded from nonthermal excitations from radioactive decay, thus the EC features will be weaker. Features dominated by Ni show variations in the region between 6.4 and 8.5 μm and weak variation at longer wavelengths, for example at 10.5 μm.

One major effect of the mixing can be seen in the 6.5–7.4 μm region. In the unmixed models, the EC and radioactive elements are mostly separate, leading to weak spectral features. This is due to the locally trapped positrons dominating the excitation in the EC region, with γ-rays being responsible for $\sim$10% of the excited ions (Penney & Hoeflich 2014). In turn, microscopic mixing produces narrow features—for example, [Ni II] at 6.636 μm has a half-width of $\approx$4000 km s^{-1}, determined by the numerical resolution. In contrast, the observed broad features suggest the central ignition of the WD.

The broad feature at $\sim$9.0 μm, dominated by Ar, is a strong diagnostic of the point of the DDT. Ar is located in a shell with a large central hole, because it is destroyed in moderately high-density burning environments ($\rho \gtrsim 1$–2×10^7 g cm^{-3}). Our model (Figure 8) is consistent with the estimates for the minimum Ar velocity, strongly suggesting a high-mass WD. The [Ar III] 8.991 μm feature shows the same slope as the [Co III] 11.888 μm feature, providing evidence of an off-center DDT.

The line profiles are strongly affected by the ionization balance. For normal SNe Ia at this phase, IGEs are typically

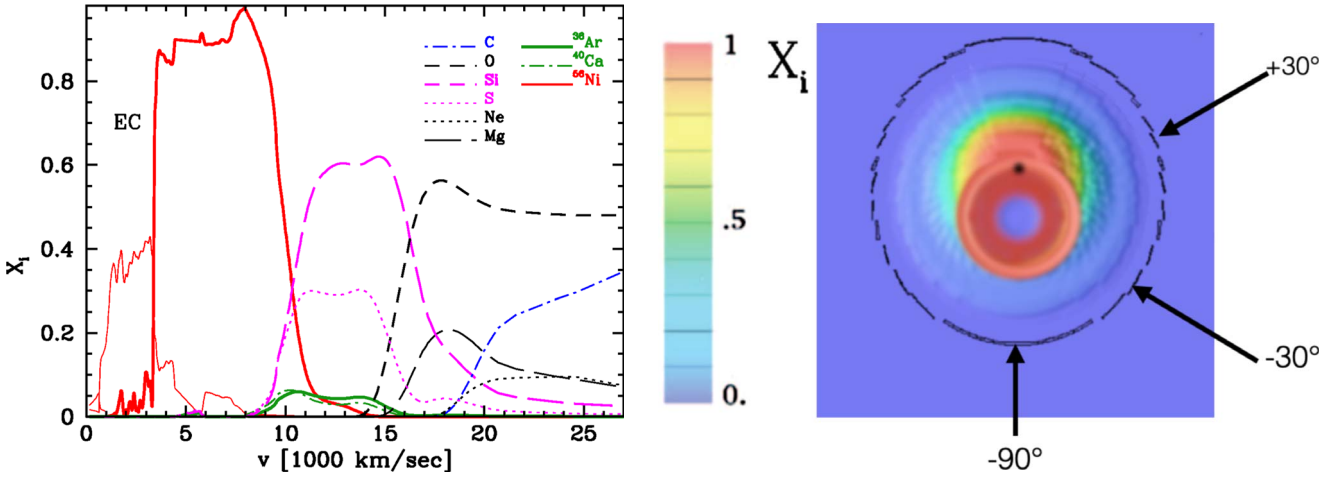

Figure 7. Left: the chemical composition of our best-fit model, Model 25, from Hoeflich et al. (2017) and Hoeflich et al. (2023). The model has chemically stratified ejecta. EC elements—e.g., ^{58}Ni with M(^{58}Ni) $\approx 5.9 \times 10^{-2}\ M_{\odot}$—are located in the center of the ejecta, followed by ^{56}Ni, farther out in velocity space. The Ar distribution goes between 8000 and 15,000 km s^{-1}, and the lightest elements (e.g., O and C) are located in the outermost layers. For illustration, the thin red line at expansion velocities larger than 3200 km s^{-1} shows the EC distribution after microscopic mixing has been applied (see the text). Right: the distributions of the IGEs of the off-center delayed detonation Model 25 at a point (the black dot). The bulk of the ^{56}Ni is in a ringlike structure between 3000 and 9500 km s^{-1} as well as in a bulge that is produced at the point of the delayed detonation transition. Depending upon the viewing angle, differently shaped line profiles will be produced in the [Co III] feature. These profiles are shown in Figure 8.

dominated by doubly ionized ions, and the ionization fraction decreases with increasing density, because the recombination rate scales with the square of the density. Only in the center, at the 10% level, do we see the effects of singly ionized IGEs that produce a strong resonance [Ni I] feature at $\approx 3\ \mu$m (Fisher 2022; Kwok et al. 2023). In the line-forming regions, the ionization balance hardly changes. Therefore, our results are insensitive to differences in the ionization structure. More detailed discussions are given in Hoeflich et al. (2021), Wilk et al. (2020), and in Section 6.1.

In the synthetic spectrum, the feature at $\sim 11.9\ \mu$m agrees well with the observations: it is dominated by [Co III] 11.888 μm and has minor line blends of [Ni I] 12.001 μm and [Co I] 12.255 μm in the red wing, at the 1% level, relative to the [Co III] peak (see the line strengths given in Table 2).

However, our models tend to show features from singly ionized elements that are too strong, by about 10%–20%, as can be seen from the ratio of the [Co III] 11.888 μm and the [Co II] 10.523 μm plus [Ni II] 10.682 μm blend. The discrepancies in the ionization balance are not unexpected, due to uncertainties in the atomic data and the $\sim$2%–5% accuracy of the flux calibration of the observed spectrum (see Section 3). Uncertain ionization and excitation by nonthermal leptons as well as uncertainties in the recombination rates lead to ionization balance uncertainties. Though we treat the cascades in energy within our Monte Carlo scheme, missing and uncertain atomic levels are likely responsible for some of the discrepancies (Wilk et al. 2018; Shingles et al. 2020; and see Appendix A of Hoeflich et al. 2021).

Finally, we discuss other observables obtainable at higher spectral resolution that may support our interpretation. Off-center delayed detonation models predict an offset between the EC elements (e.g., ^{58}Ni) that are produced during the deflagration phase and the elements (e.g., ^{56}Ni, Fe, Co, Si, S, and Ar) that are synthesized during the detonation. The former are created in a subsonic deflagration, resulting in the slow pre-expansion phase of the WD, with an almost spherical density structure, whereas the latter are formed in a weak detonation, with a burning speed close to the speed of sound. This offset may be seen with higher-resolution spectra.

Note that the unresolved small flux variations near 11 μm and in the wavelength range 12–14 μm that are seen in the MIR spectra are at a 1σ level—if confirmed by MRS spectra, these will have important implications. The computational results indicate that these small variations signal the presence of a caustic structure, in density and abundance, in the inner EC core, as has been observed by Fesen et al. (2007) and Fesen et al. (2015). At this epoch, positrons remain local for the high B field required (Penney & Hoeflich 2014; Hristov et al. 2021; Mera Evans et al. 2022).

6.4. Alternative Explosion Scenarios

A detailed discussion of the explosion scenarios and progenitor systems of SNe Ia is beyond the scope of this work. For reviews, we refer to Alsabti & Murdin (2017) and Hoeflich et al. (2021). The total mass of the exploding WD is one of the parameters that separates the different explosion scenarios, such as He-triggered detonations of sub-$M_{\rm Ch}$ WDs, dynamical mergers, violent mergers, collisions of two WDs in a triple system, and $M_{\rm Ch}$ explosions. Dynamical mergers go through a loosely bound hydrostatic WD state and are unlikely to synthesize EC elements, because the peak density during merging is too low (Benz et al. 1990; García-Berro et al. 2017). Collisions of two WDs may result in high-density burning and high masses, and they may produce EC elements; but they also produce large polarization signatures and a 90° flip in the polarization angle (Höflich 1995; Bulla et al. 2016), both of which have not been observed in any SNe Ia (Cikota et al. 2019). Similarly, violent mergers would be expected to yield high continuum polarization ($\sim$1%) at $\sim$10 days before the B-band maximum light (Bulla et al. 2016), which has also not been seen in observations (Yang et al. 2020; Patra et al. 2022).

Therefore, we focus on sub-$M_{\rm Ch}$ He-triggered detonations of C/O WDs, as an alternative viable candidate for producing SN 2021aefx. For normal SNe Ia, sub-$M_{\rm Ch}$ models have WD

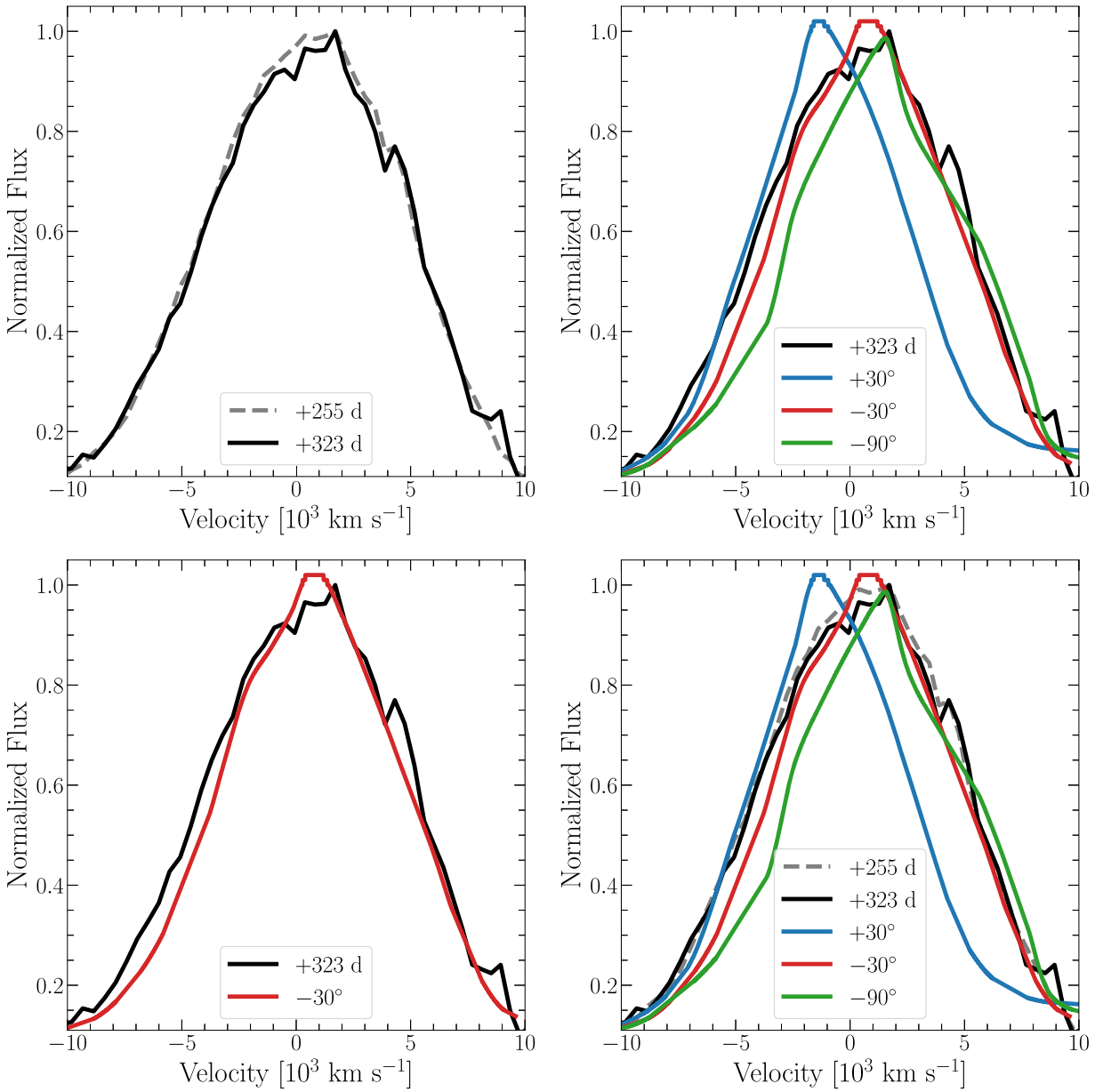

Figure 8. Top left: comparison of the [Co III] 11.888 μm line profile at +255 (dashed gray) and +323 days (solid black). Top right: dependence of the [Co III] 11.888 μm line profile as a function of inclination in comparison with the +323 day spectrum (solid black). Note that the profile and the redshift of the observed peak are consistent with the off-center DDT model as seen at −30° (bottom left), while the −30° model is also the best fit to both observations (bottom right).

masses of 1–1.05 $M_\odot$ and for bright SNe Ia they have WD masses up to 1.1 $M_\odot$ (Shen et al. 2018; Blondin et al. 2022).

Stable Ni has been identified in observations of several SN Ia, based upon the heavily blended optical and NIR features (e.g., Maguire et al. 2018; Mazzali et al. 2020); however, the Ni in these features is never the dominant line. The 1.94 μm [Ni II] line may also be present in some SNe Ia (Friesen et al. 2014; Dhawan et al. 2018; Hoeflich et al. 2021). However, this line is located at the edge of a telluric region, and it has not been seen with different reductions of the same data (see, e.g., Dhawan et al. 2018; Diamond et al. 2018). Stable Ni has also been identified in the MIR spectra of some SNe Ia (Gerardy et al. 2007; Telesco et al. 2015), albeit at low S/N. However, JWST spectra firmly establish the presence of stable Ni in SN 2021aefx, through multiple ionization states that are the dominant ions in their features, thus affirming that stable Ni exists in at least some SNe Ia (Kwok et al. 2023). The presence of EC elements strongly suggests a high-mass progenitor, even within He-triggered detonations.

In the absence of detailed spectral models, we use as a guide the ^{58}Ni mass, $\approx 5.9 \times 10^{-2}$ $M_\odot$, obtained in our simulations. Although the overall abundances and density structures of various scenarios are similar, we note that the actual value of ^{58}Ni depends on the details of the structure and, possibly, the microscopic mixing. For an $M_{\rm Ch}$ progenitor, strong microscopic mixing can be excluded, because it destroys the spectral fits (Figure 9). We note that even larger uncertainties in M(^{58}Ni) can be expected in one-zone models (Flörs et al. 2020), because they do not take into account variations in the chemical or density distributions in the inner layers and they assume that each ion has a free density, meaning that the ionization balance and level populations are not calculated

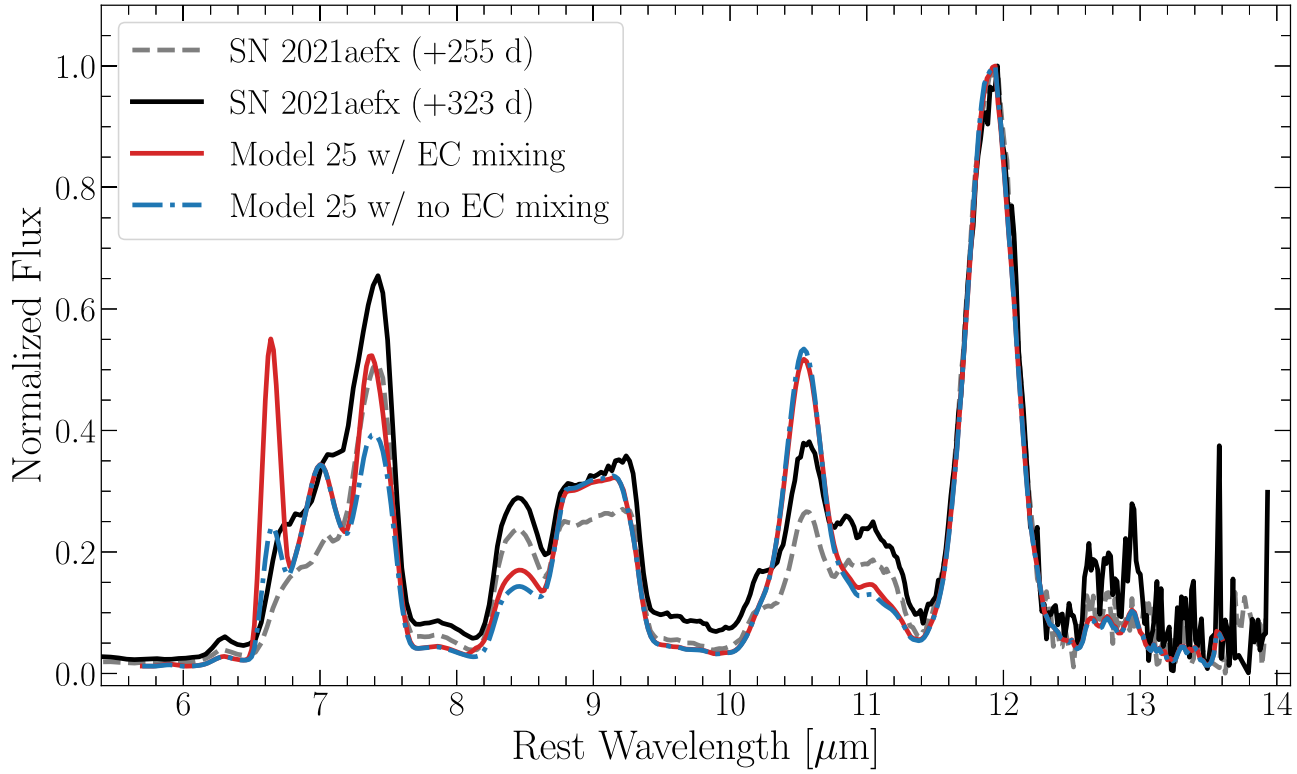

Figure 9. Comparison of the synthetic MIR spectrum of the off-center Model 25, seen from −30°, without (blue) and with (red) mixing of the EC elements (see Figure 6) and the JWST/MIRI LRS spectrum of SN 2021aefx at +255 (dashed gray) and +323 (solid black) days relative to the *B*-band maximum. The angle-averaged spectra would look similar, but they would show a flat-topped, rather than a flat-tilted, [Ar III] 8.991 μm feature. Though [Ni II] lines are present in both the synthetic spectra, the sensitivity to microscopic mixing should be noted. In particular, the [Ni II] 6.6 μm line shows a strong variation with mixing (see the text).

self-consistently. Homogeneous abundances are unlike typical explosion models for SNe Ia, and would require artificial mixing not to be expected in pure detonations. For a sub-$M_{\rm Ch}$ explosion, the EC and ^{56}Ni regions are produced in situ, and show boosted stable Ni line strengths, but they would not produce the asymmetric line profiles of [Ar III] and [Co III], nor the correct width of the [Co III] feature. All three of these considerations point to the high likelihood of SN 2021aefx originating from an $M_{\rm Ch}$ explosion.

Stable Ni is produced in NSE by shifting the ratio Y_e from ≈0.5 to a lower value, either by EC under high-density burning or in a WD with supersolar metallicities, as a result of an initial high ^{22}Ne abundance (see, for example, Brachwitz et al. 2000; Timmes et al. 2003; Thielemann et al. 2018). Gronow et al. (2021) simulate a variety of He detonation explosions at various metallicities, with various He shell masses. They find that supersolar metallicities produce EC elements, due to the decreased Y_e resulting from the presence of neutron-rich ^{22}Ne. Gronow et al. (2021) find that WDs with masses of ∼1.1 $M_\odot$ and primordial metallicities of $3Z_\odot$ produce 0.046 $M_\odot$ of stable Ni, the amount of ^{58}Ni that is sufficient to produce the strong Ni features observed in SN 2021aefx. However, since this result is due to the primordial metallicity of the WD, which reduced the Y_e uniformly throughout the WD, the full half-widths of the [Co III] line and the Ni features should be comparable, because both ^{56}Ni and ^{58}Ni are formed in the same NSE region and constant Y_e results in a constant isotopic ratio. Future MIRI/MRS observations will be able to resolve the Ni lines and accurately measure its elemental distribution. In particular, in these sub-$M_{\rm Ch}$ models, the [Ni IV] should be broad, as the high ionization stage will occur in the low-density, high-velocity region of the envelope, because the recombination rates scale with the density squared (Osterbrock & Ferland 2006). Moreover, the model that produces the large ^{58}Ni abundance requires an He shell of 0.02 $M_\odot$. Finally, if large stable Ni abundances are ubiquitous to all SNe Ia within the sub-$M_{\rm Ch}$ paradigm, this would require all of them to have supersolar metallicity, which is unlikely.

Based on recent 3D simulations of solar metallicities, Boos et al. (2021) have shown that a thin He-triggered detonation in a 1.1 $M_\odot$ C/O WD may produce 0.02 $M_\odot$ of stable Ni, an amount that is insufficient to explain the observed NIR features from stable Ni (see Wilk et al. 2020).[35]

For both sets of He detonation simulations discussed above, the mass of the outer He layers may also be inconsistent with recent limits from other early-time normal SNe Ia spectra, which show carbon in the outer 2–5 × 10^{-3} $M_\odot$ (Yang et al. 2020; Hoeflich et al. 2023). Furthermore, thin He detonation models have nearly spherical ^{56}Ni distributions (Fesen et al. 2007; Hoeflich et al. 2023), which contradict the observations of SN 2021aefx.

Lacking advanced He-triggered detonation models, we focus on spherical explosion models with sub-$M_{\rm Ch}$ cores, such as DET2 (Hoeflich & Khokhlov 1996). This model has a pure C/O WD, without an He surface layer. It originates from a WD whose mass is 1.2 $M_\odot$ and it produces a sufficient amount of

[35] Blondin et al. (2022) claim that sub-$M_{\rm Ch}$ models with $M > 1$ $M_\odot$ can produce the NIR [Ni II] lines at late times. They argue that the lack of [Ni II] in the NIR at earlier times could simply be an ionization effect, with the mixing of radioactive products in the EC region dramatically reducing the strength of the [Ni II], thus providing an option for the absence of the observed NIR [Ni II] feature. However, this explanation is inconsistent with the fact that many ionization stages of Ni are observed in SN 2021aefx.

EC material. Strict limits on the WD mass and the density of the central region can be obtained from both the [Ar III] 8.991 μm and [Co III] 11.888 μm features. In particular, a tight mass limit on the WD can be obtained via the width of the flat-top component of the [Ar III] 8.991 μm feature. The observed edges of the Ar profiles imply a central hole of Ar between $\sim$0 and 8000 km s^{-1} (see Figure 4). However, DET2 produces an inner hole of Ar of 6000 km s^{-1}. This is 2000 km s^{-1} lower than observed. To produce a wider flat-topped Ar feature would require a higher-mass WD. In a high-mass model (such as a near-$M_{\rm Ch}$ explosion), the Ar hole extends farther out in velocity space.

We note that, as an upper limit, detonating a WD with ejecta mass of 1.38 $M_{\odot}$ would mostly produce ^{56}Ni and a few QSE elements, resulting in an SN that would produce too much ^{56}Ni, would be too bright at maximum light, and would have spectra that would be inconsistent with those of a typical SN Ia (Hoeflich et al. 1996; Marquardt et al. 2015).

The velocity extent of the Ar hole would require a C/O WD of $\approx$1.24 $M_{\odot}$, from HYDRA simulations. From stellar evolution (Straniero et al. 2016), a C/O core with a maximum mass of 1.2 $M_{\odot}$ is produced by stars with a main-sequence mass of $\approx$8 $M_{\odot}$. For more massive progenitors, burning continues beyond He, resulting in O/Ne/Mg WDs and core-collapse SNe (see, for example, Woosley & Baron 1992). Alternatively, O/Ne/Mg WDs that accrete material from a companion end their lives in accretion-induced collapse to a neutron star (Woosley & Baron 1992; Wasserburg et al. 1996), because the compression will not reach the temperatures in excess of $\approx 3 \times 10^9$ K that are needed to trigger explosive O burning. In the case of C/O detonation produced via an external trigger (i.e., disruption by a black hole; Rosswog et al. 2009b), thermonuclear burning would result in a low-velocity explosion, with expansion velocities that are smaller by a factor of 2–3 compared to typical SNe Ia (Hoeflich 2017). Thus, such C/O WDs can only be produced via accretion over a long time (Kippenhahn et al. 2013). This is, however, inconsistent with the progenitor evolution channel that is commonly assumed for He shell detonations (Woosley et al. 1980; Nomoto 1982; Hoeflich & Khokhlov 1996; Shen et al. 2018).

7. Conclusion

The successful launch of JWST heralds a new era in our understanding of the physics of thermonuclear SNe. Late-nebular-phase MIR studies of SNe Ia are now possible, thanks to JWST's impressive sensitivity, obtaining spectra with higher S/Ns and at higher resolutions than any prior MIR observatory that is capable of observing SNe Ia.

Here, we present a JWST/MIRI LRS spectrum of SN 2021aefx at +323 days after maximum light, obtained through JWST program GO-JWST-2114 (PI: C. Ashall). We show how a single spectrum can be used to extract previously unavailable information about SNe Ia. We demonstrate how the natures of these important astrophysical objects can be determined by combining JWST data with spectral models. Below, we highlight our most important results.

1. The observed spectrum of SN 2021aefx is linked to the physics of SNe Ia through the construction of multi-dimensional radiation hydrodynamical NLTE models. We show that the spectrum and line profiles can be understood within the context of a delayed detonation $M_{\rm Ch}$ model, which produced an asymmetric ^{56}Ni distribution originating from a WD with a central density of $\rho_c \approx 1.1 \times 10^9$ g cm^{-3}. Although it is at the brighter end of the distribution, the model for SN 2021aefx fits within the model series, which reproduces the light curves, the luminosity–width relations, and spectra of typical SNe Ia (Section 6.2).
2. These models are used to identify the spectral lines that comprise the main features seen in the observed spectrum. The main lines that we identify include: [Co III] 11.888 μm, [Ar III] 8.991 μm, [Ni IV] 8.945 μm, [Ni I] 7.507 μm, and [Ni III] 7.349 μm. Weaker identifiable blends include lines of: [Ar II], [Fe II], [Fe III], [Co II], and [Ni II] (see Section 2).
3. The presence of multiple Ni lines in the observed spectrum demonstrates that EC elements (e.g., ^{58}Ni) are present in the inner region of SN 2021aefx. Significant amounts of these elements can only be produced by high-density burning (above 5×10^8 g cm^{-3}). These densities are found in C/O WDs with masses above $\sim$ 1.2 $M_{\odot}$. Such massive WDs must be produced via accretion (see Section 5).
4. We find evidence for no, or very limited, mixing on microscopic scales between the EC elements and the ^{56}Ni region in the ejecta. In the context of near-$M_{\rm Ch}$ models, this suggests a central point of ignition (see Section 6.3.2). Our simulations of SN 2021aefx suggest that $\sim$0.06 $M_{\odot}$ of stable Ni was produced in the explosion. In fact, since the synthetic Ni lines appear to be slightly too weak (Figure 9), we may need slightly more stable Ni than our simulations imply. The inclusion of mixing would not result in better agreement between the model and observations, as it would alter the ionization balance of the Ni lines.
5. Both the [Co III] 11.888 μm and [Ar III] 8.991 μm features show flat-tilted profiles, which vary by 10% in flux across their peaks (see Section 5). These profiles are consistent with a central hole in the corresponding element distributions. The profiles also indicate that the explosion is seen at an inclination of -30° relative to the point of the DDT (see Section 6.3.1).
6. We demonstrate how a flat-tilted profile can be used as a tool for determining the EC element and the Ar distribution within the ejecta. The length of the flat-top component corresponds to the Doppler shift of the inner hole in the element distribution, and the measured velocity extent corresponds to the average projected expansion velocity of the hole (see Section 5.1).
7. By combining information about both the strengths and profiles of the Ar and stable Ni features, we show that SN 2021aefx was most likely produced from a C/O WD with mass $>$1.2 $M_{\odot}$. This makes an He detonation sub-$M_{\rm Ch}$ explosion an unlikely candidate for this SN. SN 2021aefx appears to be a normal SN Ia, with typical light curves and spectra. We cannot rule out supersolar metallicity in sub-$M_{\rm Ch}$ WDs as an alternative option for producing EC elements in SN 2021aefx, but such models would not produce a large enough hole in the Ar region or the line profiles to reproduce the observations of SN 2021aefx. Furthermore, we regard an He detonation as unlikely, due to the fact that they produce spherical cores (e.g., ^{56}Ni distributions) that are not seen in

SN 2021aefx and are also inconsistent with the carbon-rich surfaces that are commonly seen in normal SNe Ia (see Section 6.4).

Although the data presented in this work have larger errors in wavelength calibration than anticipated, most aspects of the physical interpretation present here are insensitive to this error. For example, the off-center nature of the DDT is driven by the shapes of the line profiles. Moving forward, the improved wavelength calibration of the JWST pipeline, additional MIRI/LRS data (from program 2072; PI: S. Jha), and future MIRI/MRS data (from program 2114; PI: C. Ashall) will allow us to further constrain the physics of SN 2021aefx and other SNe Ia, and could validate our interpretation. In particular, MIRI/MRS observations will improve the precision of the data, by probing the SN ejecta to scales smaller than $\sim$100 km s^{-1}, which is essential. This MRS data will also extend to longer wavelengths ($\sim$20 μm), revealing different lines and ions, as well as allowing us to identify weaker features, by resolving many of the blends seen in the LRS spectra. It will also open a new window to probe for smaller-scale effects, such as mixing and positron transport within the ejecta at later times.

Overall, this work demonstrates the ability and potential of JWST MIR spectral observations to provide previously inaccessible information to the scientific community. This new information will allow us to determine the progenitor scenario and explosion mechanism(s) of SNe Ia. As the sample size of MIR spectra grows over the coming years, we will be able to look for diversity within the SNe Ia population.

J.D., C.A., P.H., and E.B. acknowledge support from NASA grant No. JWST-GO-02114.032-A. Support for program #2114 was provided by NASA through a grant from the Space Telescope Science Institute, which is operated by the Association of Universities for Research in Astronomy, Inc., under NASA contract NAS 5-03127. P.H. acknowledges support from the National Science Foundation (NSF), through grant No. AST-1715133. E.B. acknowledges support from NASA grant No. 80NSSC20K0538. This publication was made possible by the support of an LSSTC Catalyst Fellowship to K.A.B., funded through grant No. 62192 from the John Templeton Foundation to the LSST Corporation. The opinions expressed in this publication are those of the author(s) and do not necessarily reflect the views of LSSTC or the John Templeton Foundation. I.D. acknowledges partial support from the Spanish project PID2021-123110NB-100, financed by MCIN/AEI/10.13039/501100011033/FEDER/UE. L.G. acknowledges financial support from the Spanish Ministerio de Ciencia e Innovación (MCIN), from the Agencia Estatal de Investigación (AEI), 10.13039/501100011033, from the European Social Fund (ESF), "Investing in your future," under the 2019 Ramón y Cajal program RYC2019-027683-I and the PID2020-115253GA-I00 HOSTFLOWS project, from Centro Superior de Investigaciones Científicas (CSIC), under PIE project No. 20215AT016, and from the program Unidad de Excelencia María de Maeztu CEX2020-001058-M. The research of Y.Y. is supported through a Bengier–Winslow–Robertson Fellowship. S.W.J. and L.A.K. acknowledge support from NASA grant No. JWST-GO-02072.001 and NASA FINESST fellowship 80NSSC22K1599. This work is based on observations made with the NASA/ESA/CSA James Webb Space Telescope. The data were obtained from the Mikulski Archive for Space Telescopes at the Space Telescope Science Institute, which is operated by the Association of Universities for Research in Astronomy, Inc., under NASA contract NAS 5-03127 for JWST. These observations are associated with program #2114. The specific observations analyzed in this work can be accessed via DOI 10.17909/6fjc-sx91.

Facilities: JWST (LRS/MIRI), MAST (JWST),the simulations presented here were performed on the Beowulf system of the Astrophysics Group at Florida State University.

Software: jwst (ver. 1.8.1; Bushouse et al. 2022), HYDRA (Höflich 2003, 2009; Hoeflich et al. 2017), OpenDx (an open-sourced visualization package developed by IBM), `SNooPy` (Burns et al. 2011, 2014), Astropy (Astropy Collaboration et al. 2013, 2022; Price-Whelan et al. 2018), NumPy (Harris et al. 2020), SciPy (Virtanen et al. 2020), Matplotlib (Hunter 2007).

Appendix
NIR Line Identifications from Model 25

Line identifications, as determined from Model 25 in the NIR are listed in Table 4.

Table 4
NIR Model Line Identifications

S	λ (μm)	Ion	S	λ (μm)	Ion	S	λ (μm)	Ion	S	λ (μm)	Ion	S	λ (μm)	Ion
**	2.211	[Fe II]	***	2.478	[Fe II]	*	2.935	[Co II]		3.169	[Fe III]	***	4.076	[Fe II]
***	2.219	[Fe III]	*	2.479	[Ni II]	*	2.954	[Co I]		3.185	[Fe III]	*	4.077	[Fe III]
*	2.219	[Fe III]		2.481	[Co I]	**	2.961	[Fe II]	*	3.187	[Co II]	**	4.082	[Fe II]
***	2.243	[Fe III]		2.493	[Fe III]		2.963	[Fe III]	***	3.230	[Fe III]		4.108	[Co I]
*	2.243	[Fe III]		2.506	[Co I]		2.965	[Fe III]		3.230	[Fe III]	***	4.115	[Fe II]
***	2.244	[Fe II]	**	2.515	[Fe II]		2.966	[Fe III]	*	3.239	[Co II]	*	4.307	[Co II]
**	2.257	[Fe II]	*	2.526	[Co I]		2.987	[Fe III]		3.242	[Fe III]		4.340	[Co I]
**	2.267	[Fe II]	*	2.531	[Co II]		3.006	[Co I]		3.286	[Co II]		4.357	[Fe III]
**	2.281	[Co III]		2.570	[Fe III]		3.012	[Co II]		3.332	[Co I]		4.357	[Fe III]
*	2.282	[Co II]		2.581	[Co I]	*	3.014	[Co III]		3.353	[Co I]	*	4.410	[Co II]
	2.284	[Co I]	*	2.601	[Co II]	*	3.014	[Co II]	*	3.394	[Ni III]	**	4.435	[Fe II]
	2.285	[Co I]	*	2.652	[Co I]		3.017	[Fe III]		3.471	[Co I]	*	4.520	[Ni I]
	2.297	[Co I]		2.686	[Co I]		3.018	[Fe III]	*	3.492	[Co III]	***	4.608	[Fe II]
**	2.309	[Ni II]	*	2.692	[Co II]	*	3.031	[Co I]		3.498	[Fe III]	*	4.672	[Fe II]
	2.316	[Co I]	**	2.717	[Fe III]	***	3.044	[Fe III]	*	3.630	[Co II]	*	4.788	[Ni I]
*	2.335	[Ni II]		2.717	[Fe III]		3.044	[Fe III]	*	3.633	[Co I]		4.860	[Fe III]
	2.348	[Co I]		2.726	[Co I]		3.046	[Co I]		3.647	[Co I]	***	4.889	[Fe II]
***	2.349	[Fe III]	*	2.767	[Co II]		3.061	[Co I]		3.655	[Co I]		5.054	[Co I]
*	2.349	[Fe III]		2.833	[Co I]		3.063	[Fe III]	*	3.659	[Co II]	**	5.062	[Fe II]
*	2.361	[Ni II]	*	2.839	[Co II]		3.085	[Fe III]	*	3.705	[Co II]		5.164	[Co I]
**	2.370	[Ni II]	*	2.848	[Co II]		3.085	[Fe III]		3.738	[Co I]	*	5.180	[Co II]
***	2.371	[Fe II]	*	2.871	[Co I]		3.095	[Fe III]		3.750	[Co I]	**	5.187	[Ni II]
	2.411	[Fe III]	***	2.874	[Fe III]		3.097	[Fe III]	*	3.752	[Co II]		5.211	[Co I]
*	2.414	[Co I]		2.874	[Fe III]		3.100	[Fe III]		3.771	[Co I]	***	5.340	[Fe II]
	2.447	[Fe III]	*	2.889	[Co II]	*	3.100	[Co II]	*	3.802	[Ni III]	**	5.674	[Fe II]
*	2.453	[Fe III]	***	2.905	[Fe III]		3.120	[Co I]		3.823	[Co I]	**	5.704	[Co II]
	2.453	[Fe III]		2.905	[Fe III]	***	3.120	[Ni I]	*	3.849	[Co II]	**	5.893	[Ni I]
**	2.474	[Co III]	**	2.911	[Ni II]		3.129	[Fe III]		3.877	[Co I]	*	5.940	[Co II]
*	2.477	[Co II]	*	2.933	[Co II]	*	3.151	[Co II]	**	3.952	[Ni I]	*	5.953	[Ni II]

Note. For each transition, the markers correspond to strong (***), moderate (**), weak (*), and scarcely detectable ( ), on top of the quasi-continuum formed by a large number of lines. The relative strength S is estimated by the integral over the envelope, $\int A_{ij} n_j \, dV$, where n_j is the particle density of the upper level.

ORCID iDs

J. M. DerKacy https://orcid.org/0000-0002-7566-6080
C. Ashall https://orcid.org/0000-0002-5221-7557
P. Hoeflich https://orcid.org/0000-0002-4338-6586
E. Baron https://orcid.org/0000-0001-5393-1608
B. J. Shappee https://orcid.org/0000-0003-4631-1149
D. Baade https://orcid.org/0000-0003-1637-9679
J. Andrews https://orcid.org/0000-0003-0123-0062
K. A. Bostroem https://orcid.org/0000-0002-4924-444X
P. J. Brown https://orcid.org/0000-0001-6272-5507
C. R. Burns https://orcid.org/0000-0003-4625-6629
A. Burrow https://orcid.org/0000-0002-5380-0816
A. Cikota https://orcid.org/0000-0001-7101-9831
T. de Jaeger https://orcid.org/0000-0001-6069-1139
A. Do https://orcid.org/0000-0003-3429-7845
Y. Dong https://orcid.org/0000-0002-7937-6371
I. Dominguez https://orcid.org/0000-0002-3827-4731
L. Galbany https://orcid.org/0000-0002-1296-6887
E. Y. Hsiao https://orcid.org/0000-0003-1039-2928
E. Karamehmetoglu https://orcid.org/0000-0001-6209-838X
K. Krisciunas https://orcid.org/0000-0002-6650-694X
S. Kumar https://orcid.org/0000-0001-8367-7591
J. Lu https://orcid.org/0000-0002-3900-1452
T. B. Mera Evans https://orcid.org/0000-0001-5888-2542
J. R. Maund https://orcid.org/0000-0003-0733-7215
P. Mazzali https://orcid.org/0000-0001-6876-8284
K. Medler https://orcid.org/0000-0001-7186-105X
N. Morrell https://orcid.org/0000-0003-2535-3091
F. Patat https://orcid.org/0000-0002-0537-3573
M. M. Phillips https://orcid.org/0000-0003-2734-0796
M. Shahbandeh https://orcid.org/0000-0002-9301-5302
S. Stangl https://orcid.org/0000-0001-5570-6666
C. P. Stevens https://orcid.org/0000-0003-0763-6004
M. D. Stritzinger https://orcid.org/0000-0002-5571-1833
N. B. Suntzeff https://orcid.org/0000-0002-8102-181X
C. M. Telesco https://orcid.org/0000-0002-0036-9292
M. A. Tucker https://orcid.org/0000-0002-2471-8442
S. Valenti https://orcid.org/0000-0001-8818-0795
L. Wang https://orcid.org/0000-0001-7092-9374
Y. Yang https://orcid.org/0000-0002-6535-8500
S. W. Jha https://orcid.org/0000-0001-8738-6011
L. A. Kwok https://orcid.org/0000-0003-3108-1328

References

Allison, J. R., Sadler, E. M., & Meekin, A. M. 2014, MNRAS, 440, 696
Alsabti, A. W., & Murdin, P. 2017, Handbook of Supernovae (Berlin: Springer)
Ashall, C., Hoeflich, P., Hsiao, E. Y., et al. 2019b, ApJ, 878, 86
Ashall, C., Hsiao, E. Y., Hoeflich, P., et al. 2019a, ApJL, 875, L14
Ashall, C., Lu, J., Shappee, B. J., et al. 2022, ApJL, 932, L2
Astropy Collaboration, Price-Whelan, A. M., Lim, P. L., et al. 2022, ApJ, 935, 167
Astropy Collaboration, Robitaille, T. P., Tollerud, E. J., et al. 2013, A&A, 558, A33

Axelrod, T. S. 1980, PhD thesis, Univ. California, Santa Cruz
Beals, C. S. 1929, MNRAS, 90, 202
Benz, W., Cameron, A. G. W., Press, W. H., & Bowers, R. L. 1990, ApJ, 348, 647
Blondin, S., Bravo, E., Timmes, F. X., Dessart, L., & Hillier, D. J. 2022, A&A, 660, A96
Boos, S. J., Townsley, D. M., Shen, K. J., Caldwell, S., & Miles, B. J. 2021, ApJ, 919, 126
Bostroem, K. A., Jha, S. W., Randriamampandry, S., et al. 2021, TNSCR, 2021-3888, 1
Botyánszki, J., & Kasen, D. 2017, ApJ, 845, 176
Brachwitz, F., Dean, D. J., Hix, W. R., et al. 2000, ApJ, 536, 934
Branch, D., & Wheeler, J. C. 2017, Supernova Explosions (Berlin: Springer)
Burns, C., Hsiao, E., Suntzeff, N., et al. 2021, ATel, 14441, 1
Bulla, M., Sim, S. A., Pakmor, R., et al. 2016, MNRAS, 455, 1060
Burns, C. R., Stritzinger, M., Phillips, M. M., et al. 2011, AJ, 141, 19
Burns, C. R., Stritzinger, M., Phillips, M. M., et al. 2014, ApJ, 789, 32
Bushouse, H., Eisenhamer, J., Dencheva, N., et al. 2022, WST Calibration Pipeline, v1.8.1, Zenodo, doi:10.5281/zenodo.7215690
Calder, A. C., Plewa, T., Vladimirova, N., Lamb, D. Q., & Truran, J. W. 2004, arXiv:astro-ph/0405162
Chandrasekhar, S. 1939, An Introduction to the Study of Stellar Structure (Chicago, IL: Univ. of Chicago press)
Cikota, A., Patat, F., Wang, L., et al. 2019, MNRAS, 490, 578
Dhawan, S., Flors, A., Leibundgut, B., et al. 2018, A&A, 619, A102
Diamond, T. R., Hoeflich, P., & Gerardy, C. L. 2015, ApJ, 806, 107
Diamond, T. R., Hoeflich, P., Hsiao, E. Y., et al. 2018, ApJ, 861, 119
Elagali, A., Staveley-Smith, L., Rhee, J., et al. 2019, MNRAS, 487, 2797
Fesen, R. A., Höflich, P. A., Hamilton, A. J. S., et al. 2007, ApJ, 658, 396
Fesen, R. A., Höflich, P. A., & Hamilton, A. J. S. 2015, ApJ, 804, 140
Fisher, A. 2022, PhD thesis, Florida State Univ.
Flörs, A., Spyromilio, J., Taubenberger, S., et al. 2020, MNRAS, 491, 2902
Fransson, C., & Jerkstrand, A. 2015, ApJL, 814, L2
Fransson, C. 1994, in Supernovae. NATO Advanced Science Institutes (ASI) Series C: Mathematical and Physical Sciences. Proc. of the 54th École d'été de physique théorique, session LIV, ed. S. A. Bludman, R. Mochkovitch, & J. Zinn-Justin (Amsterdam: Elsevier), 677
Friesen, B., Baron, E., Wisniewski, J. P., et al. 2014, ApJ, 792, 120
Gamezo, V. N., Khokhlov, A. M., & Oran, E. S. 2005, ApJ, 623, 337
Gamezo, V. N., Khokhlov, A. M., Oran, E. S., Chtchelkanova, A. Y., & Rosenberg, R. O. 2003, Sci, 299, 77
García-Berro, E., Badenes, C., Aznar-Siguán, G., & Lorén-Aguilar, P. 2017, MNRAS, 468, 4815
Gerardy, C. L., Meikle, W. P. S., Kotak, R., et al. 2007, ApJ, 661, 995
Gordon, K. D., Bohlin, R., Sloan, G. C., et al. 2022, AJ, 163, 267
Graham, M. L., Kumar, S., Hosseinzadeh, G., et al. 2017, MNRAS, 472, 3437
Gronow, S., Côté, B., Lach, F., et al. 2021, A&A, 656, A94
Harris, C. R., Millman, K. J., van der Walt, S. J., et al. 2020, Natur, 585, 357
Hoeflich, P. 2017, in Handbook of Supernovae, ed. A. W. Alsabti & P. Murdin (Berlin: Springer), 1151
Hoeflich, P., Ashall, C., Bose, S., et al. 2021, ApJ, 922, 186
Hoeflich, P., Hsiao, E. Y., Ashall, C., et al. 2017, ApJ, 846, 58
Hoeflich, P., & Khokhlov, A. 1996, ApJ, 457, 500
Hoeflich, P., Mueller, E., & Khokhlov, A. 1991, A&A, 248, L7
Hoeflich, P., Wheeler, J. C., Hines, D. C., & Trammell, S. R. 1996, ApJ, 459, 307
Hoeflich, P., Yang, Y., Baade, D., et al. 2023, MNRAS, 520, 560
Höflich, P. 1995, ApJ, 440, 821
Höflich, P. 2003, in ASP Conf. Ser. 288, Stellar Atmosphere Modeling, ed. I. Hubeny, D. Mihalas, & K. Werner (San Francisco, CA: ASP), 185
Höflich, P. 2009, in AIP Conf. Ser. 1171, Recent Directions in Astrophysical Quantitative Spectroscopy and Radiation Hydrodynamics, ed. I. Hubeny et al. (Melville, NY: AIP), 161
Höflich, P., Gerardy, C. L., Fesen, R. A., & Sakai, S. 2002, ApJ, 568, 791
Höflich, P., Gerardy, C. L., Marion, H., & Quimby, R. 2006, NewAR, 50, 470
Höflich, P., Khokhlov, A. M., & Wheeler, J. C. 1995, ApJ, 444, 831
Höflich, P., & Stein, J. 2002, ApJ, 568, 779
Höflich, P., Wheeler, J. C., & Thielemann, F. K. 1998, ApJ, 495, 617
Hosseinzadeh, G., Sand, D. J., Lundqvist, P., et al. 2022, ApJL, 933, L45
Hoyle, F., & Fowler, W. A. 1960, ApJ, 132, 565
Hristov, B., Collins, D. C., Hoeflich, P., Weatherford, C. A., & Diamond, T. R. 2018, ApJ, 858, 13
Hristov, B., Hoeflich, P., & Collins, D. C. 2021, ApJ, 923, 210
Hsiao, E. Y., Marion, G. H., Phillips, M. M., et al. 2013, ApJ, 766, 72
Hunter, J. D. 2007, CSE, 9, 90
Iben, I., Jr., & Tutukov, A. V. 1984, ApJS, 54, 335
Jha, S. W., Maguire, K., & Sullivan, M. 2019, NatAs, 3, 706
Kasen, D. 2006, ApJ, 649, 939
Kendrew, S., Scheithauer, S., Bouchet, P., et al. 2015, PASP, 127, 623
Khokhlov, A. M. 1991a, A&A, 245, L25
Khokhlov, A. M. 1991b, A&A, 245, 114
Kippenhahn, R., Weigert, A., & Weiss, A. 2013, Stellar Structure and Evolution (Berlin: Springer)
Kozma, C., & Fransson, C. 1992, ApJ, 390, 602
Kumar, S., Hsiao, E. Y., Ashall, C., et al. 2022, arXiv:2210.06993
Kushnir, D., Katz, B., Dong, S., Livne, E., & Fernandez, R. 2013, ApJL, 778, L37
Kwok, L. A., Jha, S. W., Temim, T., et al. 2023, ApJL, 944, L3
Livne, E., & Arnett, D. 1995, ApJ, 452, 62
Livne, E. 1999, ApJL, 527, L97
Livne, E., Asida, S. M., & Höflich, P. 2005, ApJ, 632, 443
Lu, J., Hsiao, E. Y., Phillips, M. M., et al. 2022, arXiv:2211.05998
Ma, H., Woosley, S. E., Malone, C. M., Almgren, A., & Bell, J. 2013, ApJ, 771, 58
MacEwen, H. A., Fazio, G. G., Lystrup, M., et al. 2016, Proc. SPIE, 9904, 990443
Maguire, K., Sim, S. A., Shingles, L., et al. 2018, MNRAS, 477, 3567
Maoz, D., Mannucci, F., & Nelemans, G. 2014, ARA&A, 52, 107
Marion, G. H., Höflich, P., Gerardy, C. L., et al. 2009, AJ, 138, 727
Marquardt, K. S., Sim, S. A., Ruiter, A. J., et al. 2015, A&A, 580, A118
Mazzali, P. A., Bikmaev, I., Sunyaev, R., et al. 2020, MNRAS, 494, 2809
Mazzali, P. A., Ropke, F. K., Benetti, S., & Hillebrandt, W. 2007, Sci, 315, 825
Mazzali, P. A., Sullivan, M., Filippenko, A. V., et al. 2015, MNRAS, 450, 2631
Meikle, W. P. S., Spyromilio, J., Allen, D. A., Varani, G. F., & Cumming, R. J. 1993, MNRAS, 261, 535
Menzel, D. H. 1929, PASP, 41, 344
Mera Evans, T. B., Hoeflich, P., & Diehl, R. 2022, ApJ, 930, 107
Mihalas, D. 1978, Stellar Atmospheres (2nd ed.; Freeman: Freeman)
Morrison, P., & Sartori, L. 1966, PhRvL, 16, 414
Nienmeyer, J. C., Hillebrandt, W., & Woosley, S. E. 1996, ApJ, 471, 903
Nomoto, K. 1982, ApJ, 257, 780
Nomoto, K., Thielemann, F.-., & Yokoi, K. 1984, ApJ, 286, 644
Osterbrock, D. E., & Ferland, G. J. 2006, Astrophysics of Gaseous Nebulae and Active Galactic Nuclei (Sausalito, CA: Univ. Science Books)
Pakmor, R., Kromer, M., Taubenberger, S., et al. 2012, ApJL, 747, L10
Pakmor, R., Kromer, M., Taubenberger, S., & Springel, V. 2013, ApJL, 770, L8
Patra, K. C., Yang, Y., Brink, T. G., et al. 2022, MNRAS, 509, 4058
Penney, R., & Hoeflich, P. 2014, ApJ, 795, 84
Perlmutter, S., Aldering, G., Goldhaber, G., et al. 1999, ApJ, 517, 565
Phillips, M. M. 1993, ApJL, 413, L105
Piersanti, L., Gagliardi, S., Iben, I. J., & Tornambé, A. 2003a, ApJ, 583, 885
Piersanti, L., Gagliardi, S., Iben, I. J., & Tornambé, A. 2003b, ApJ, 598, 1229
Poludnenko, A. Y., Chambers, J., Ahmed, K., Gamezo, V. N., & Taylor, B. D. 2019, Sci, 366, aau7365
Price-Whelan, A. M., Crawford, S., Sipőcz, B., et al. 2018, Astropy/Astropy-V2.0-Paper: Final Draft Zenodo, doi:10.3847/1538-3881/aac387
Riess, A. G., Filippenko, A. V., Challis, P., et al. 1998, AJ, 116, 1009
Riess, A. G., Macri, L. M., Hoffmann, S. L., et al. 2016, ApJ, 826, 56
Riess, A. G., Rodney, S. A., Scolnic, D. M., et al. 2018, ApJ, 853, 126
Rigby, J., Perrin, M., McElwain, M., et al. 2022, arXiv:2207.05632
Röpke, F. K., Woosley, S. E., & Hillebrandt, W. 2007, ApJ, 660, 1344
Rosswog, S., Kasen, D., Guillochon, J., & Ramirez-Ruiz, E. 2009a, ApJL, 705, L128
Rosswog, S., Ramirez-Ruiz, E., & Hix, W. R. 2009b, ApJ, 695, 404
Seitenzahl, I. R., & Townsley, D. M. 2017, in Handbook of Supernovae, ed. A. W. Alsabti & P. Murdin (Berlin: Springer), 1955
Shen, K. J., Kasen, D., Miles, B. J., & Townsley, D. M. 2018, ApJ, 854, 52
Shingles, L. J., Sim, S. A., Kromer, M., et al. 2020, MNRAS, 492, 2029
Spencer, L. V., & Fano, U. 1954, PhRv, 93, 1172
Straniero, O., Piersanti, L., & Cristallo, S. 2016, JPhCS, 665, 012008
Struve, O. 1931, ApJ, 74, 225
Tartaglia, L., Sand, D. J., Valenti, S., et al. 2018, ApJ, 853, 62
Telesco, C. M., Höflich, P., Li, D., et al. 2015, ApJ, 798, 93
Thielemann, F., Isern, J., Perego, A., & von Ballmoos, P. 2018, SSRv, 214, 62
Thompson, T. A. 2011, ApJ, 741, 82
Timmes, F. X., Brown, E. F., & Truran, J. W. 2003, ApJL, 590, L83
Van Hoof, P. 2018, Galax, 6, 63
Virtanen, P., Gommers, R., Oliphant, T. E., et al. 2020, NatMe, 17, 261
Wasserburg, G. J., Busso, M., & Gallino, R. 1996, ApJL, 466, L109

Webbink, R. F. 1984, ApJ, 277, 355
Wheeler, J. C., Höflich, P., Harkness, R. P., & Spyromilio, J. 1998, ApJ, 496, 908
Whelan, J., & Iben, I., Jr 1973, ApJ, 186, 1007
Wilk, K. D., Hillier, D. J., & Dessart, L. 2018, MNRAS, 474, 3187
Wilk, K. D., Hillier, D. J., & Dessart, L. 2020, MNRAS, 494, 2221
Woosley, S. E., & Baron, E. 1992, ApJ, 391, 228
Woosley, S. E., & Weaver, T. A. 1994, ApJ, 423, 371
Woosley, S. E., Weaver, T. A., & Taam, R. E. 1980, in Texas Workshop on Type I Supernovae, Proc. of the Texas Workshop, ed. J. C. Wheeler (Austin, TX: Univ. of Texas), 96
Yang, Y., Hoeflich, P., Baade, D., et al. 2020, ApJ, 902, 46